EUROPEAN ORGANIZATION FOR NUCLEAR RESEARCH

CERN-PPE/93-131
July 20, 1993

A NEW SEARCH FOR $\nu_\mu - \nu_\tau$ OSCILLATION

CHORUS Collaboration

M. de Jong, J. Konijn, C.A.F.J. van der Poel, J.L. Visschers : **NIKHEF, Amsterdam**
E. Arik, E. Eskut, A.A. Mailov, G. Onengüt, E. Pesen, M. Serin-Zeyrek, R. Sever,
P. Tolun, M.T. Zeyrek : **YEFAM, Ankara, Turkey**
N. Armenise, M.G. Catanesi, M.T. Muciaccia, S. Simone : **INFN and University of Bari, Bari**
K. Höpfner, P. Lendermann, T. Patzak : **Humboldt University, Berlin**
M. Gruwé, C. Mommaert, P. Vilain, G. Wilquet : **IIHE (ULB-VUB), Brussels**
C.H. Hahn : **Changwon National University, Changwon, Korea**
J.Y. Kim, I.T. Lim : **Chonnam National University, Chonnam, Korea**
E. Di Capua, C. Luppi, S. Ricciardi, B. Saitta, P. Zucchelli :
INFN and University of Ferrara, Ferrara
M. Kazuno, H. Shibuya : **Toho University, Funabashi, Japan**
R. Beyer, J. Brunner, J.P. Fabre, R. Ferreira, W. Flegel, R. Meijer Drees, H. Øverås, J. Panman,
A. Rozanov, G. Stefanini, K. Winter, H. Wong : **CERN, Geneva**
K. Nakazawa: **Gifu University, Gifu, Japan**
H. Chikawa : **Kinki University, Higashiosaka, Japan**
K.S. Chung, I.G. Park, J.S. Song : **Gyeongsang National University, Jinju, Korea**
K. Kodama, N. Ushida : **Aichi University of Education, Kariya, Japan**
S. Aoki, T. Hara : **Kobe University, Kobe, Japan**
D. Favart, G. Gregoire, X. Lauwerys, V. Lemaitre, L. Michel: **Université Catholique de Louvain, Louvain-la-Neuve**
A. Artamonov, P. Gorbunov, V. Khovansky, V. Shamanov, V. Smirnitsky : ITEP, Moscow
D. Frekers, H. von Heynitz : **Münster University, Münster**
K. Hoshino, M. Kobayashi, M. Nakamura, Y. Nakamura, K. Niu, K. Niwa, T. Nakano, O. Sato :
Nagoya University, Nagoya, Japan
K. Nakamura, T. Okusawa, M. Teranaka : **Osaka City University, Osaka, Japan**
S. Buontempo, A. Cocco, A. Ereditato, G. Fiorillo, F. Marchetti-Stasi, V. Palladino, F. Riccardi,
P. Strolin : **INFN and University of Naples, Naples**
G. Baroni, A.Capone, D. de Pedis, S. Di Liberti, U. Dore, P.F. Loverre, D. Macina, M.A. Mazzoni,
F. Meddi, G. Piredda, G. Rosa, R. Santacesaria : **INFN and University of Rome, Rome**
G. Grella, G. Romano : **INFN and University of Salerno, Salerno**
Y. Sato, I. Tezuka : **Utsunomiya University, Utsunomiya, Japan**

Abstract

This report is describing the status of the construction of the WA95-CHORUS detector. It supersedes the text of the proposal CERN-SPSC/90-42 SPSC P254 which was approved by the CERN Research Board in September 1991.

Table of Contents

1. INTRODUCTION

The question whether neutrino flavours mix at some level and the related question whether neutrinos have non-zero mass is one of the remaining great challenges of experimental high energy physics. A new search for $\nu_\mu - \nu_\tau$ oscillations has recently received incentives from the solar neutrino experiments. Combining the results of the Davis Chlorine experiment [1], the Kamiokande neutrino-electron scattering experiment [2] and results from GALLEX [4] and SAGE (Soviet-American-Gallium-Experiment) [3], a consistent description by a MSW solution seems to be a possible explanation of the solar neutrino problem [5]. The cosmological connection between neutrino masses and the enigma of dark matter has been invoked by Harari [6]. The COBE-IRAS data seem to prefer a mixed dark matter scenario with $m_{\nu_\tau} \sim 7$ eV. None of these considerations is compelling; however, they suggest that $\nu_\mu - \nu_\tau$ oscillation may be within reach of a new experiment which we will perform at the CERN-SPS [7]. We shall perform the experiment in the wide band neutrino beam facility of the CERN-SPS to explore the domain of small mixing angles down to $\sin^2 2\theta_{\mu\tau} \sim 3 \times 10^{-4}$ for mass parameters $\Delta m^2 > 1$ eV^2. The region of sensitivity of this new experiment and those already explored previously are shown in figure 1. If oscillations would occur at the present limit ($\sin^2 2\theta_{\mu\tau} = 5 \times 10^{-3}$, $\Delta m^2 > 50$ eV^2) we would observe 64 events in the proposed experiment.

The improvement of this new search for $\nu_\mu - \nu_\tau$ oscillation is based on three important elements which contribute in an essential way to its feasibility :

(1) the increase of emulsion target mass and the intense ν_μ beam of the CERN-SPS neutrino facility,

(2) detection of the reaction $\nu_\tau N \rightarrow \tau^- X$ with three different subsequent decay modes, $\tau^- \rightarrow \mu^- \bar{\nu}_\mu \nu_\tau$, $\tau^- \rightarrow h^- (n\,\pi^\circ)\,\nu_\tau$, and $\tau^- \rightarrow (\pi^+ \pi^- \pi^-)\,(n\,\pi^\circ)\,\nu_\tau$,

(3) reduction of the number of events to be scanned in the emulsion by a factor of ~ 10 by kinematical selection.

In the following sections we describe the conceptual design of the experiment, the elements of the detector, the neutrino beam, the analysis and the background estimates. The beam time estimate and the time schedule are given at the end.

II. CONCEPTUAL DESIGN OF THE EXPERIMENT

The search for $\nu_\mu - \nu_\tau$ oscillation will be performed by detecting the occurrence of the inclusive reaction

$$\nu_\tau N \rightarrow \tau^- X \qquad (1)$$

in a background of ν_μ induced charged (CC) and neutral current (NC) events. We are aiming at a statistical sensitivity at the 90% confidence limit of $\sin^2 2\theta_{\mu\tau} \cong 3 \times 10^{-4}$. At 450 GeV proton energy the flux of prompt ν_τ produced via D_s meson production and decay is much lower than the ν_μ flux; we

estimate a ratio of ~ 10^{-7} (see SectionV.3). Background from other sources will occur at a level of 10^{-7} per ν_μ charged current (CC) interaction, $N^{CC}(\nu_\mu)$.

The best limit up to now, $\sin^2 2\theta < 4 \times 10^{-3}$ (see figure 1) was established by the experiment E531 at FNAL [8] using an emulsion-counter hybrid detector. The CHARM II experiment has recently set a 90% confidence limit at $\sin^2 2\theta_{\mu\tau} < 6.4 \times 10^{-3}$ using different techniques. The proposed experiment aims at improving the sensitivity by a factor of more than twenty.

The conceptual design of the experiment we are preparing is based on the detection of the characteristic decay topology of the short lived τ lepton and on kinematical constraints based on the missing p_T of the undetected ν_τ in tau decays.

A proven technique for this detection is the nuclear emulsion with a resolution of ~ 1 μm. To make the increase of sensitivity possible and to keep at the same time the number of events to be scanned in the emulsion reasonably small, we shall detect the decay mode $\tau^- \rightarrow \mu^- \bar{\nu}_\mu \nu_\tau$ which has a branching ratio of 17.8%, the decay mode $\tau^- \rightarrow h^- (n\,\pi^0)\,\nu_\tau$ which has a branching ratio of 50.3%, and the decay mode $\tau^- \rightarrow (\pi^+ \pi^- \pi^-)\,(n\,\pi^0)\,\nu_\tau$ with a branching ratio of 13.8%. An electronic detector composed of arrays of 10^6 scintillating fibres, a magnetic spectrometer, a high resolution calorimeter and a muon spectrometer (figure 2) is used to select events with a negative muon or a negative pion and missing transverse momentum, and locates the events to be scanned in the emulsion by extrapolating the tracks (see Section V.2) back to the exit point at the emulsion. The large number of ν_μ induced charged current or neutral current interactions which would have to be scanned if no distinction from the ν_τ induced reaction (1) were possible, will be reduced by selecting candidates for reaction (1) on the basis of their characteristically different kinematics. This will be discussed in detail in Section V.1.

Although this selection reduces the detection efficiency for reaction (1) as well, it is the most effective method to achieve the sensitivity we are aiming at.

The decay mode $\tau^- \rightarrow \mu^- \bar{\nu}_\mu \nu_\tau$ is particularly clean and the main background due to charm production is low. The identification and the measurement of the muon charge and momentum is made with high efficiency downstream of the target array.

Decay modes of the τ lepton into a single charged hadron and ν_τ have a larger branching ratio and can, therefore, add to the sensitivity of the experiment. We shall select events without a muon but with a negative hadron in a certain kinematical range and with the help of a magnetic spectrometer, located immediately behind the target and the tracking section, again to keep the number of events to be scanned in the emulsion small. The main background for this mode is due to quasi elastic scattering of a negative hadron near the vertex without a visible recoil track. This background can be studied with high statistics using data of this experiment. Our present knowledge [see Section V.3] indicates that it can be reduced by selecting candidates which have a decay track with transverse momentum, with respect to the τ direction, $p_T > 0.24$ GeV/c.

The decay mode of the tau into three charged pions does not impose a stringent selection on the momentum of the pion. Requiring a minimum number (e.g. ≥ 2) of negatively charged hadrons in the event, is reducing significantly the events to be scanned in the emulsion [see Section V.3]. The

contribution of the main source of background - the diffraction dissociation of negative pions - can be reduced by suitable kinematical cuts and determined within the experiment.

Because of the observation of the decay topology in coincidence with the kinematical selection and the independence of the formation in 3 different decay channels we are confident that we can obtain a sensitivity to the mixing parameter down to or below 3×10^{-4} or, in the case we observe some candidates, significant measurement of the signal.

For candidate events we can test whether the tau track candidate does balance the transverse momenta of the hadron shower. Using this test we can enhance their statistical significance (see Section V.4)

We also plan to build and to test a prototype of a scintillating fibre target to gain experience with this new technique. Should this test exposure be successful it would be possible to build a complete detector based on this technique for continuing the search for $\nu_\mu \leftrightarrow \nu_\tau$ oscillations and for the detection of the reaction $\nu_\tau N \rightarrow \tau^- X$ in a tau neutrino beam.

In the following paragraphs we describe the elements of this detector and their performance.

III. THE DETECTOR DESIGN

III.1. Emulsion Stacks

The emulsion target has a total volume of 230 litres and a total mass of 800 kg. It is segmented into two times 2 stacks of 1.44×1.44 m^2 surface area, each of 2.75 cm thickness. Each stack will be subdivided into 8 sectors of 0.71×0.36 m^2; the sectors will be composed of 25 emulsion layers. Particle track directions are nearly perpendicular to the emulsion sheets. This configuration permits fast semiautomatic and automatic scanning, techniques which have been developed over the past 10 years at Nagoya University [8, 9]. The emulsion layers (2×550 μm thick) are deposited onto the two faces of a 90 μm thick acetate rayon foil. Three auxiliary emulsion sheets are mounted in front of the first fibre tracker plane (see figure 3). The tracks measured with the fibre trackers predict the track position in two adjacent special sheets within an area of $(300\ \mu m)^2$ and provide an angular resolution of $\Delta\theta \sim 3$ mrad. Automatic scanning of the sheets will reduce the track position to an area of $(1\ \mu m)^2$ and from both sheets together the angular definition to $\Delta\theta \sim 0.2$ mrad. These sheets will be replaced every three weeks during running time of the experiment to provide favourable background conditions for the recognition of the predicted tracks in the emulsion. The combination of fibre trackers and emulsion sheets thus provides good time resolution in correlating tracks from kinematically selected events with high space resolution. Each stack will be vacuum packed and positioned inside a rigid frame which also holds the changeable emulsion sheets and the scintillating fibre array.

In order to handle high multiplicity events in the fibre tracker following the emulsion, a distance of 40 mm and 50 mm between the target bulk emulsion and the two changeable sheets (CS1 and CS2) is required. Another fixed emulsion sheet (SS in figure 3), similar to the changeable sheets, is positioned close to the bulk emulsion. A scanning area of $(10\ \mu m)^2$ on this sheet is predicted from the changeable sheets; the track position will be determined in an area of $(1\ \mu m)^2$. In this way, high scanning efficiency in the bulk emulsion can be achieved to overcome the high track density.

Following exposure and development, the emulsion layers will be cut into slices of 7×7 cm^2 surface area, each. As is shown in figure 4, slices from successive layers will be mounted onto a plastic backing thus forming a tower type geometry of events which can be automatically scanned without changing plates. The microscope stages are positioned by computer control to the predicted location of the selected track impact point. The system follows this track into the emulsion, finds the production vertex (~ 15 minutes) and searches for a decay kink angle larger than 10 mrad along the tracks leaving the vertex (figure 3) between 20 μm and 3 mm from the vertex (~ 5 minutes). A total of ~ 40'000 events has to be scanned in this way.

With the semiautomatic scanning tables now available in the collaboration institutes this scanning will take about one year.

The emulsion stacks are kept at a temperature of 5 °C in a cool box covering the whole target area, the hexagonal magnet, and the associated fibre trackers (see figure 2). In this way the unavoidable process of fading of the emulsion is controlled, and a lifetime of two years is achieved.

III.2. Scintillating Fibre Tracker

The emulsion targets are followed by scintillating fibre tracking devices which provide a precise prediction of the tracks on the changeable emulsion sheet (figure 3).

Two emulsion stacks, separated by a pair of changeable sheets and a scintillating fibre tracking detector, are followed by a drift space in which three scintillating fibre trackers are positioned. The first of these three planes is placed as close as possible to another pair of changeable sheets. This sequence is repeated for the other two emulsion stacks.

Each scintillating fibre tracker provides a measurement in 4-projections y, z, y',z' to determine an unambiguous space track. The projections y' and z' are rotated by an angle of 8° with respect to y and z; the sense of the rotation is alternating between +8° and -8° in successive planes. Track recognition is obtained with the help of the three trackers in the drift space. The tracker interspersed between two emulsion stacks provides a precise extrapolation of tracks into the upstream stack and avoids tedious emulsion scanning to follow tracks through the downstream emulsion stack. The tracking system is designed to predict the position of the most favourable tracks at the exit face of the emulsion within an area of (300 μm)^2 with high efficiency, and to provide an angular measurement of about 3 mrad. Good two track resolution is required to handle the large particle densities close to the interaction vertex. The track detector is compact to avoid loss of accuracy by extrapolating tracks over too large distances.

Each tracker projection is composed of ribbons of 500 μm diameter scintillating fibres[1] arranged in seven staggered layers (figure 5) with a pitch of one-half fibre diameter and with a total scintillator thickness of 3.2 mm to ensure good efficiency. The fibres have a cladding of 3 μm thickness. Each layer is covered with a TiO_2 - based white paint acting as a glue and as an extra-mural absorber.

---

(1) Fibers SCSF-38 manufactured by Kuraray, Japan

This arrangement provides good two-track resolution, adequate precision to locate tracks in the emulsion (see figure 3), and favourable conditions for pattern recognition in the drift space with three space points for each track.

Three additional fibre trackers of hexagonal shape are placed one directly upstream and two downstream of the hexagonal magnet (see III.3). The last coordinate plane of the target region and the first hexagonal plane are spaced by 40 cm and provide a high precision angle measurement before the magnet. The deflection in the magnet is measured with two hexagonal trackers, downstream of the magnet. Four auxiliary streamer tube planes follow these trackers to ensure sufficient pattern recognition and good timing.

Each hexagonal tracker is composed of six diamond-shaped fibre modules, and provides two coordinate measurements per track. The fibres are arranged at an angle of 60° with respect to each other (see figure 6). The fibres and their arrangement are identical to those of the target tracker.

One end of the fibre is covered with a sputtered aluminium mirror of ~80% reflectivity. The other ends of the ribbons are bundled together, are polished and 16 of them are coupled to the photo cathode of the first image intensifier (see figure 7). The performance of these fibre ribbons has been tested in a pion beam (see figure 8). We obtain on average 3 photoelectrons per mm of fibre traversed at the far end of the fibre. The sigma of the track residual is 140 μm and that for the two track resolution is 200 μm. This allows us to obtain two coordinates per 3 mm thick layer with excellent efficiency for point reconstruction on tracks.

Specifications of the various fibre tracker planes are summarised in Table 1.

Table 1
Summary of fibre trackers

type	fibres/ projection	max. fibre* length	number of projection	total* length
Z or Y	22400	2.3 m	16	824 km
Z' or Y'	22400	2.5 m	16	896 km
diamond	18200	2.6 m	18	824 km

The total fibre length required is 2600 km and the total number of image intensifier chains is 58.

III.3. Optoelectronical readout of fibres

The fibres of all trackers are bundled and coupled to image intensifiers which are read-out by CCD's (see figure 9). The image intensifier chain is composed of a large surface demagnifying stage (100 mm diameter to 25 mm diameter) with low gain and high quantum efficiency(1), followed by a

* including 70 cm for light guides

(1) Hamamatsu

second electrostatic device which increases the gain[2] , a high gain gated microchannel plate[3] (MCP), and a final demagnifying stage[2] (25 mm to 11 mm diameter) coupled to a CCD with 550×288 pixels. The total demagnification is 9.1 providing 6 pixels per fibre.

A slow phosphor (P11) with a decay time constant of 50 μs for 50% of the light is used for the first image intensifiers, followed by fast phosphors (P46) to allow for a 500 ns trigger decision time without excessive loss of light output. A gate length of 20 μs contains 36% of the light at the photo cathode of the MCP.

The first event within one spill from the SPS is stored in the memory region of the CCD (frame store), the following events are kept in the sensitive region. The resulting overlay probability is estimated at 6.5% based on an average trigger rate per spill (10^{13} p) of 0.75 event. They can be disentangled with the help of the other detector elements. The system thus provides a buffer capacity of at least 2×2 events per accelerator cycle.

III.4. Hexagonal Magnet

An air core magnet is located between the target region and the calorimeter to determine the charge and the momentum of particles before they enter the calorimeter. Severe constraints are imposed on the magnet design. A stray field would prohibit the use of electrostatic image intensifiers for the fibre trackers, and complicate the tracking unnecessarily. The magnet length is restricted to keep a large acceptance for the downstream calorimeter and spectrometer; the amount of material traversed by particles should be minimised.

A hexagonal magnet has been built satisfying these conditions. It is made of six equal-sided triangles with 1.5 m sides, 0.75 m depth. It has been built inside a cylinder with 3.6 m diameter (see figure 10). Windings of thin aluminium sheet cover all faces of the triangles, producing a homogeneous field in each triangle section parallel to the outer side. The field strength has no radial dependence.

The material of the front and back faces represent $\lesssim 4\%$ of a radiation length each. The six spokes of the magnet, formed by two sides of adjacent triangles, represent dead space for momentum reconstruction. Averaged over all charged tracks with momentum between 2.5 and 10 GeV/c the acceptance of the magnet is 85%. Because of the time structure of the neutrino beam the magnet-current is pulsed with a duty-factor of $\sim 4 \times 10^{-3}$. A field of 0.12 T is reached using standard CERN rectifiers and the power dissipation is 15 kW. Because of the dense packing of detectors in front and behind the magnet this heat has to be cooled by blowing cold air along the conductors at the inside of each magnet triangle. The warmed-up air is then collected and evacuated to the outside of the cool box.

Combining the errors of the direction measurements before and behind the magnet one obtains a total measurement error of

---

(2) DEP

(3) Proxitronix

$$\left(\frac{\Delta p}{p}\right)_{\text{measurement}} = 1.6\ \% \cdot p/(\text{GeV/c})$$

multiple scattering gives a momentum independent contribution of $\left(\frac{\Delta p}{p}\right)_{\text{m.sc.}} = 16\ \%$. Combining them quadratically (see figure 11) one obtains a momentum resolution varying between 16% (p = 2 GeV/c) and 23% (p = 10 GeV/c), sufficient to determine the sign of the charge with more than 8 st. dev. for particles up to 10 GeV/c. The momentum measurement will be used to determine the transverse momentum of pions and to predict the range of low energy (1-2 GeV/c) muons.

III.5. Streamer Tube Trackers

CHARM II streamer tubes will be used for pattern recognition purposes upstream of the veto scintillators and the calorimeter, interspersed between the calorimeter segments, in front of the muon spectrometer, and in the gaps of the muon spectrometer (see figure 2).

In the spectrometer the streamer tube planes are arranged in groups of eight, four with vertical and four horizontal wires. The wire spacing is 1 cm, and the cathode strip spacing is 2.1 cm. For the muon spectrometer there is an analogue read-out of the cathode strips and a digital read-out of the wires. Thus, one group provides 16 coordinate measurements. The precision of the wire read-out in the muon spectrometer is improved by drift-time measurements on groups of eight wires, giving a precision of $\sigma \sim$ 1 mm.

The other planes are only equipped with digital read-out of the wires. They are grouped in pairs inside the calorimeter and in groups of four planes upstream of the veto scintillators and the calorimeter.

III.6. High Resolution Calorimeter

An effective way of distinguishing the reactions

(i) $\nu_\tau N \rightarrow (\tau^- \rightarrow \mu^- \bar{\nu}_\mu \nu_\tau) X$, $(\tau^- \rightarrow \pi^- \nu_\tau)$ X and $(\tau^- \rightarrow \pi^+ \pi^- \pi^- (n\,\pi^\circ)\, \nu_\tau)$ X

from

(ii) $\nu_\mu N \rightarrow \mu^- X$ and $\nu_\mu N \rightarrow \nu_\mu X$

is based on detecting the missing transverse energy carried away by neutrinos in reaction (i) and to exploit the characteristic correlation of its vector with that of the hadron final state X (see Chapter V.1). To determine the hadron shower direction and energy we have built a high energy resolution calorimeter.

Showers induced in the calorimeter by individual hadrons tend to spread out and overlap. Their energy flow vectors can therefore not be obtained individually. We determine instead the energy flow vector of the whole hadron final state by measuring the centre of gravity of its energy flow in the calorimeter and connecting it to the vertex position which is measured by the fibre trackers. The modularity of the calorimeter has been chosen accordingly. Each calorimeter plane is composed of modules which are oriented laterally to measure the energy flow profile in two orthogonal projections (see figure 12a) alternating in horizontal and vertical directions. The cross sections of these modules are smaller than the shower size of charged hadrons. The error on the measurement of the centre of gravity of the energy flow is therefore determined by the fluctuations of the energy measurement. It is for this reason that we have designed a high resolution calorimeter. It is also required to give equal response for

charged and neutral pions to avoid any bias. These requirements of high resolution and equal response for neutral and charged pions can be met by a compensating lead-scintillator calorimeter with a lead to scintillator volume ratio of 4 to 1.

The secondary particles of the τ decay will have an energy on average smaller than 5 GeV, 99% (90%) containment of a 5 GeV hadronic shower requires about 5.2 (3) λ_{int}.

The CHORUS calorimeter consists of three sectors with decreasing granularity, called EM, HAD1 and HAD2. The first sector is aimed at the measurement of the energy of the electromagnetic component of the event, the first two provide the measurement of the hadronic component of the events and the third completes the latter measurement acting as a tail catcher. The volume ratio between lead and scintillator is 4 to 1 for all sectors, in order to achieve compensation. The total depth is about 5.2 λ_{int}.

The first two sectors (EM and HAD1) are made of lead and scintillating fibres and longitudinally contain 5 GeV hadron showers at the 90% level. The third sector (HAD2) is made of lead and scintillating strips (sandwich technique), as the detection of the tail shower allows a coarser space (and energy) resolution. The calorimeter consists of vertical and horizontal modules, with limited streamer tube planes in between. These tracking detectors are required to connect the tracks in the muon spectrometer following the calorimeter to those reconstructed by the scintillating fibre tracker in front of the calorimeter.

The EM sector modules are built by piling up extruded layers of grooved lead and plastic scintillating fibres of 1mm diameter positioned in the grooves (see figure 12b). A module consists of a pile of 21 layers (2620 mm long) and 740 fibres. On either side, fibres are arranged in two groups defining two different read-out cells with about 40×40 mm^2 cross-sections. These four groups are coupled via a Plexiglas light guide to a 1" photo multiplier (PM). The pile is kept together and contained in a steel box. The HAD1 modules are built in a similar way, piling up the same basic lead sheets, but 3350 mm in length. In these modules, there are 43 layers, 1554 fibres and the cross-section is approximately squared (80×80 mm^2). On either side, the fibres are grouped and coupled via a light guide to a 2" PM. For both the EM and the HAD1 modules, the light guide is required to mix the light coming out of the individual fibres. The lead/fibre pile for the HAD1 module is also contained in a steel box. The HAD2 modules, instead, are sandwiches made up of 16 mm thick extruded lead plates with 4 mm thick scintillator strips (3650 mm long) and the modules are also read-out as two cells. The strips on either side are connected to two 2" PM's (the same PM's as for HAD1) via independent light guides. The lead and scintillator strips are contained in a thin steel box.

A group of two streamer tube planes (one horizontal and the other vertical) is inserted behind each second plane of the EM sector and behind each plane of the HAD1 and HAD2 sectors (figure 12a). There is a total of 11 groups (22 planes), i.e. about 7500 streamer tubes read-out in digital mode.

The main features of the calorimeter design are summarised in Table 2 and the module cross-sections are shown in figure 12b.

The energy resolution for electromagnetic and hadronic showers was measured using lead-scintillating fibre calorimeter prototypes built by the LAA/SPACAL Collaborations, including the Naples group of CHORUS.

Table 2

Item	EM	HAD1	HAD2	Total
Module dimensions (mm^3)	$40 \times 80 \times 2620$	$80 \times 80 \times 3350$	$100 \times 200 \times 3690$	
Number of planes	4	5	5	14
Thickness X_0 (λ_{int})	21.5 (0.78)	55.2 (2.0)	67.1 (2.44)	143.8 (5.22)
Number of modules	124	200	90	414
PM's per module	4	2	4	
Total number of PM's	496	400	360	1256
Number of fibres	93000	310800	-	403800
Number of scintillator strips	-	-	900	900
Lead weight (tons)	9.7	42	60	111.7
Scintillator weight (tons)	0.22	0.92	1.32	2.46

For electrons an energy resolution of $\sigma(E_e)/E \cong 13\%/\sqrt{E}$ *(GeV)* was found, and for pions $\sigma(E_\pi)/E \cong 30\%/\sqrt{E}$ *(GeV).*

The above results for electrons have been confirmed by measurements performed on modules of the CHORUS calorimeter.

Discrimination of e/π can be achieved at a level of ~ 10^{-3} from the shower width and the energy ratio in the electromagnetic and hadronic sectors of the calorimeter. Electron tracks from converted photons can thus be excluded from the sample of tracks used for tracking back to the vertex.

The position of the centre of gravity of a hadron shower can be determined with a resolution of σ(HAD) ~ 1.5 cm at 5 GeV. Combining this with the vertex position which is determined with σ(vertex) ~ 0.3 cm we obtain a shower direction measurement resolution $\sigma(\theta_h)$ ~ 10 mrad at 5 GeV.

The calibration and monitoring of the performance of the different modules will be accomplished by using cosmic ray events taken between neutrino spills.

The calorimeter is mounted on a support standing on rails which can then be moved off the beam axis to perform a dedicated energy calibration with electron and pion beams from the SPS X7 beam line.

III.7. The Muon Spectrometer*

The muon spectrometer consists of six circularly magnetised iron modules of 375 cm diameter (see figure 13) and seven tracking sections, one in front, five in the gaps between the iron modules, and one behind. Each magnet module is constructed of twenty iron plates of 2.5 cm thickness. Coils are running through a central hole of 8 cm diameter to the outer radius; the magnetic field in the iron is close to 2 Tesla. The gaps are interleaved with 8 mm thick scintillation counters, with strips of 15 cm width, oriented, alternatively, horizontally and vertically. They are coupled to photo multipliers in groups of 5 plates. The range of muons can thus be determined with a sampling step 12.5 cm of iron.

The new tracking sections consist each of one drift chamber and eight streamer tube planes. Each drift chamber module is equipped with three planes of sense wires oriented at 0°, +60° and -60° with respect to the horizontal. The streamer tubes have a wire spacing of 1 cm and a cathode strip pitch of 2.1 cm. Drift time measurements are made for groups of eight wires and give a resolution of 1 mm.

Each tracking section thus gives 19 coordinate measurements which are combined and determine a space vector for each track. From a fit of these space vectors along the muon track the momentum is determined. The resolution depends on the number of modules traversed; a 20 GeV/c muon traversing all six modules is measured with 15% resolution; if it is traversing only one module the resolution is 30%.

The scintillation counters in the gaps of the iron magnets have four functions. They are providing trigger signals for penetrating tracks and are complementing the measurement of hadron energy leaking from the preceding hadron calorimeter. They also give the range of muons stopping in one of the modules, and they measure the energy lost by bremsstrahlung in the iron modules.

III.8. Trigger and Data Acquisition

The main task of the trigger is to select all neutrino induced events in the target and to reject background from cosmic rays, muons from the beam, and neutrino interactions outside the target. In addition, trigger modes for calibration and alignment of the detector are needed. The expected neutrino event rate is 0.75 events per spill of 10^{13} protons on target for an effective mass of 2400 kg.

The neutrino interaction trigger is using information from two hodoscope modules, one close to the target region, T1, and one just in front of the calorimeter, T2 (see figure 2). T1 is made of two layers of 15 thin scintillator strips of 10 cm width and 160 cm length, oriented horizontally. the two layers are staggered and cover an area of 160×160 cm^2. The thickness is minimised to avoid loss of tracking precision due to multiple scattering. For the same reason the planes are mounted as close as possible to

---

* Major parts of the muon spectrometer with its electronics have kindly been lent to us by the CDHS Collaboration. It is described in detail elsewhere [14]. We summarise only the main features here.

the last fibre tracker of the target region. Trigger plane T2 is made of two layers of 20 strips of 10 cm width and 200 cm length, oriented horizontally.

A veto system (V) is positioned 2 m in front of the target region and consists of two planes of twenty 20 cm wide scintillators oriented vertically, and staggered by one-half width. They form a plane of 4×3.2 m^2 surface area. An additional plane of 32 scintillators vetoes events from the concrete floor.

The neutrino interaction trigger is defined by a combination of pulses from the hodoscope strips T1 and T2 consistent with a track with $\tan(\theta) < 0.25$ with respect to the neutrino beam. A veto is formed by any combination of a veto counter hit and a hit in T1, with precise timing to avoid vetoes due to back scattering. All scintillator strips of T1 and V are viewed at both ends by photo multipliers to fulfil the timing requirements.

The size of the veto counter has been chosen to fully cover the area defined by the angular acceptance of the hodoscope trigger.

The muon flux incident on the detector located in the BEBC hall has been measured during neutrino beam operation and was found to be $N_\mu \cong 500/m^2$ for one cycle of 2×10^{13} protons. At this point of the hall the shielding is weak and has been reinforced by adding iron in front of the detector (Section IV.3). This is reducing the muon flux by a factor ~ 10. A space of about 10 m is kept between the shielding and the detector to minimise background from neutrino induced particles. The number of incident muons must be kept as low as possible to minimise background in the emulsion stacks.

After removal of beam-related incoming muon tracks, the main background is created by neutrino interactions in the surrounding material such as supports and the floor. These events can satisfy the trigger conditions if several tracks hit the hodoscopes, thereby faking one small angle track. This background is kept low by minimising heavy support structures close to the fiducial volume. Cosmic ray background is expected to be small.

Additional signals from the calorimeter and the muon spectrometer will be used to build independent pattern triggers for evaluation of the trigger efficiency, and to record neutrino interactions for beam flux monitoring.

A 4×4 m^2 streamer tube wall has been put directly upstream of the veto plane (figure 17) to define, together with a range requirement in the muon spectrometer, high momentum muon tracks for alignment and calibration.

Data Acquisition

The event rate in this experiment is low, on average less than one event per neutrino burst. Each event contains a large amount of raw data (~ 20 Mbyte fibre pixels, and ~ 10 kbytes of calorimeter, spectrometer and streamer tube data). This has to be reduced to a few hundred kbytes in a very early stage before the data is combined into one single event, to avoid the need for large bandwidth data buses. This requirement calls for simple pattern processing at the level of the conversion. A second level software trigger is not needed.

The requirement to read-out up to three or four events per burst sets the upper limit of a few hundred millisecond read-out time per event. The data volume produced is doubled by calibration and alignment triggers taken between the neutrino bursts. It is expected that data tapes will be written with a frequency of one every few hours.

The data acquisition is based on a VME-bus hardware with CPU's running the OS-9 operating system (figure 14). The heart of the system is formed by a "root" crate containing the event builder CPU, and a dual 3480 cartridge unit connected via a SCSI bus. Its task is to assemble events from the converted data in the other crates, data recording on cartridges and to send events to the UNIX cluster for sample data analysis for quality monitoring. The event data flow will be channelled through a VIC vertical bus. The video signals from the fibre trackers are digitised in the cameras and processed with dedicated CPU's. Each CPU serves two cameras. Interfaces to CAMAC for ADC and TDC modules and trigger logic, etc., are foreseen. The system is organised hierarchically with at least one VME crate and processor serving each detector sub-system.

All ADC and TDC channels are equipped with multiple event buffers and have fast conversion times less than 20 μsec. Events are stored in these buffers during the neutrino burst, and are read-out between and after them.

The data quality will be monitored with UNIX work stations connected through ethernet lines to all VME crates. They can perform sample data analysis, on-line calibration and the display of histograms prepared on the OS-9 system. Permanently updated information will be available on screens connected to the workstations.

Dead time

Trigger dead time is introduced by activity in the veto counter, by the strobe signal, by the duration of the conversion of valid events, and by the overflow of read-out buffers. The latter source can be removed by choosing sufficient buffer depth, or by overlaying events in the limited buffers of the CCD's. The expected dead time contributions are summarised in Table 3 (the effective spill length is 4 ms).

Table 3
Contribution to event losses by dead time

Source	Number per burst	Length	Dead time (fraction)
veto	400	60 ns	6×10^{-3}
pretrigger $\overline{V} \times T1 \times T2$	10	600 ns	1.5×10^{-3}
strobes from other detectors	100	60 ns	1.5×10^{-3}
MCP gate + delays	0.75	30 μs	5.6×10^{-3}
CCD conversion	0.75	120 μs	22.5×10^{-3}
ADC/TDC conversion other events	5	20 μs	25×10^{-3}
TOTAL			62×10^{-3}

We expect a total loss of events due to dead time of 6%. In addition, if we limit the maximum number of events to two, the dead time is increased by another 6.5%. This can be avoided by overlaying the second and the third event in one CCD frame.

Because of the high redundancy of the trigger system, and of the simplicity of the requirements, a trigger efficiency of 98% can be estimated for events passing the off-line selection criteria. The total detector efficiency is $\varepsilon_{det} = 92\%$.

III.9. Scintillating Fibre Target

A new detector approach is being developed based entirely on coherent arrays of thin scintillating optical light guides. This detector concept is suitable for a continued search for $\nu_\mu \leftrightarrow \nu_\tau$ oscillations at SPS-energies and for ν_τ-detection at future high energy colliders (e.g. LHC). To identify the reaction $\nu_\tau N \rightarrow \tau^- X$ a massive detector with fibres of diameter 20 μm - 100 μm will be needed.

We are adding a prototype detector module to the emulsion hybrid detector set-up to obtain experience with this novel technique. This module will be composed of 20 μm diameter fibres oriented transverse or parallel to the incident beam (see figure 15). Our specifications require a minimum of 4 detectable hits/mm on tracks crossing the far end of the fibre target. This requirement is based on a study of pattern recognition using Monte Carlo methods, which indicates that a vertex resolution of about 10 μm and a reconstruction probability of τ-decay kinks of about 20% are possible, Using fibres of 20 μm diameter [10].

The mass of the 150 cm long prototype module is ~ 1 kg and should be sufficient to collect a sample of neutrino interactions which will enable us to test the analysis chain including pattern recognition and kink detection efficiency.

We envisage using blocks of glass capillaries filled with liquid scintillator [10]. Our investigations show that in capillaries filled with liquid scintillator reflection loss give attenuation lengths larger than 1 m. The presently developed technology allows to produce submodules with sizeable dimensions ($2 \times 2 \times 150$ cm^3). Suitable liquid scintillators with high refractive index have been optimised for small self absorption and high light output.

IV. THE NEUTRINO BEAM

The CERN wide band horn focused neutrino beam has been built for the CHORUS and NOMAD experiments. Some modifications were introduced with respect to the beam layout used during CHARM II datataking. The electronics, data acquisition and control system of the NFM (Neutrino Flux Monitor) has been completely replaced by more modern equipment.

The SPS accelerates protons to 450 GeV with a cycle of 14.4.s. Protons are extracted in two 6 ms long spills separated in time by 2.5 s, one at the beginning and the other at the end of the energy flat top. They are focused onto a 3 mm diameter Be target consisting of six rods of 10 cm length each and

separated by a free space of 10 cm. With this double pulsing 10^{13} protons per spill or $2 \cdot 10^{13}$ protons per cycle can be targeted without damaging the Be rods.

The target is followed by a redesigned, tapered collimator system matching the parent beam to the horn aperture. The distance of the horn with respect to the target and the horn current influence the mean parent energy and neutrino energy. The reaction $\nu_\tau + N \rightarrow \tau^- + X$ we are searching for has a threshold of 3.5 GeV and the efficiency for detecting the tau lepton in this experiment has a threshold at ~ 8 GeV. The horn-target distance has been increased to 20 m and the horn current of 110 kA to maximise the rate of the ν_τ CC reaction.

Two successive helium filled tubes of 80 cm diameter and a total length of about 100 m are inserted between the horn and the reflector and between the reflector and the decay tunnel to reduce pion absorption.

A background of $\overline{\nu}_\mu$ in the ν_μ beam is due to parent particles of negative charge which are not strongly enough defocussed by the horn. The ratio of fluxes, $N(\overline{\nu}_\mu) / N(\nu_\mu)$ was minimised to reduce one of the background sources (see Section V.3) by introducing a new collimator behind the horn to intercept defocused negative pions before they decay.

IV.1. Neutrino spectra, beam components and event rates

The energy spectra of the different neutrino beam components are shown in figure 16. The mean energy of the ν_μ flux is 27 GeV, the abundances and mean energies of the other components are summarised in Table 4. They have been determined in the course of the CHARM II experiment [16]. Table 4 also gives the event rate for a target mass of 800 kg covering a beam area of 1.4×1.4 m^2 for 10^{19} protons on target. These numbers have been determined experimentally at the location of the CHARM II detector [16] and were scaled to the new position using a MC simulation program [17]. In the following we shall use a total number of protons on the target of 2.4×10^{19} producing 5×10^5 ν_μ induced CC events (see Section VI). The redesigned beam will give 17% higher event rate for the reaction $\nu_\tau N \rightarrow \tau X$ (see Tables 5 and 6).

Table 4

Neutrino beam components and mean energies as determined in the CHARM II experiment [16]

component	relative abundance	$\langle E_\nu \rangle$ (GeV)	CC Evts/0.8 ton $\cdot 10^{19}$ p
ν_μ	1.0	26.9 ± 0.5	2.1×10^5
$\overline{\nu}_\mu$	0.056 ± 0.004	21.7 ± 1.0	
ν_e	0.007 ± 0.0013	47.9 ± 2.2	
$\overline{\nu}_e$	0.0017 ± 0.0003	35.3 ± 1.7	

IV.2. Muon Shielding

The muon flux of 500 / $m^2 \cdot 2 \cdot 10^{13}$ p measured in the BEBC hall will be reduced by a factor of ~ 10 by means of additional shielding as in the case of the CHARM II experiment. Assuming 5000 SPS cycles per day, the muon flux shall be 0.25 / mm^2 / day, and hence, 0.5 tracks in 20 days in the "fiducial area" of the changeable sheets (300 μm × 300 μm) and 0.01 tracks in 400 days in the fiducial area (10 μm × 10 μm) of the emulsion stacks. These figures show that the flux of beam muons is completely negligible, concerning both visibility and false candidates. It must be noted, in addition, that beam muons will be used to link in a very accurate way the sheets of the emulsion stacks in order to have a single reference system.

A general survey of muons originating from hadron beams in the West Area and restriction on their use to avoid excessive background is underway.

IV.3. Detector Layout

The CHORUS detector is installed in the BEBC hall at CERN, 60 m closer to the decay tunnel than the CHARM II detector (see figure 17). The X7 beam can be sent either through the detector in its final position, or for calibration of the calorimeter in a position outside the detector.

V. DATA ANALYSIS

After reconstruction of the selected events in the scintillating fibre arrays, calorimeter and the muon spectrometer, the sample of events to be measured in the emulsion target is selected using criteria discussed in Section V.1. The procedure of emulsion scanning is presented in Section V.2. For events in which a decay kink is found additional criteria are applied to reduce the background, as explained in Section V.3.

Most of the results presented here are based on LUND-generated neutrino interactions, using the neutrino beam characteristics described in reference [17] and Section IV.1.

V. 1. Selection of ν_τ Candidate Events for Scanning

For the analysis to be performed in a reasonably short time, the number of events to be scanned in the emulsion must represent only a small fraction of the total number of ν interactions in the target. Three sets of selection criteria will be used, one to enrich the events with μ^- tracks ("CC-sample") to search for $\tau^- \rightarrow \mu^- \bar{\nu}_\mu \nu_\tau$, one to search for $\tau^- \rightarrow h^- \nu_\tau$ in events without muons ("NC-sample") and one to search for $\tau^- \rightarrow \pi^+ \pi^- \pi^-$ (n π°) ν_τ events.

CC-sample Selection

We select events with a μ^- track defined as:

1) either a negative track reconstructed in the muon spectrometer

2) or a negative track of energy > 1 GeV, stopping in the calorimeter preceding the spectrometer and for which the momentum measured in the air core magnet is compatible with the one deduced from the observed range.

In both cases, the muon candidate has to be linked with a track originating in the emulsion.

No other candidate must be detected with an energy $\gtrsim 1$ GeV. This requirement eliminates most of the charm-induced dimuon events. Further reduction of the sample is obtained by exploiting the kinematical features which differentiate ν_τ from ν_μ charged current interactions:

1) a lower mean muon momentum (figure 18) for the ν_τ reaction, $p_\mu < 30$ GeV/c;

2) an unbalanced (missing) transverse momentum (figure 19) because of the undetected neutrinos in $\tau \rightarrow \mu\nu_\mu\nu_\tau$ decay, p_T (miss) > 0.4 GeV/c;

3) the missing transverse momentum tends to be opposite to the hadronic transverse momentum (figure 20) in ν_τ reactions and nearly symmetric in ν_μ reactions, $\Phi(p_T \text{(hadron)} - p_T \text{(miss)}) > 90°$;

Figures 18 to 20 show that even if detector resolution effects and Fermi motion are taken into account, these features are still observable. In addition, visibility cuts at the τ decay vertex are applied as discussed in Section V.2.

Table 5 summarises the effects of the proposed cuts on three samples of simulated events:

$$\nu_\tau + N \rightarrow \tau^- + X \qquad (1)$$
$$\hookrightarrow \mu^- \bar{\nu}_\mu \nu_\tau$$

$$\nu_\mu + N \rightarrow \mu^- + X \qquad (2)$$

$$\bar{\nu}_\mu + N \rightarrow \mu^- + D^- + X \qquad (3)$$
$$\hookrightarrow \mu^- + \text{neutrals}$$

Other criteria aim at a reduction of the contribution of background processes:
A decay with a kink angle > 10 mrad at a distance of 20 μm to 3 mm from vertex, a $p_T^{decay} > 0.24$ GeV/c with respect to the direction of the decaying track found in the emulsion, and rejection of events with a visible μ^+.

The geometrical acceptance (μ^- seen), muon tracking efficiency (μ^- tracking) and the accidental event loss because of a hadron simulating a μ^+ track (μ^+ punch through) further reduce the sample.

Finally, there is the detector efficiency (ε_{det}), a safety factor for the neutrino flux (ε_{beam}) which we are now putting to 1 (one) because of the increased event rate of the redesigned neutrino beam and the

scanning efficiency (Table 5). Including also the neutrino flux weighted rates of $N_\tau = \int \sigma_\tau \, (dN/dE_\nu) dE_\nu$ and $N_\mu = \int \sigma_\mu \, (dN/dE_\nu) dE_\nu$ with a ratio of $N_\tau/N_\mu = 0.51$ and the branching ratio $BR(\tau^- \to \mu^- \bar{\nu}_\mu \nu_\tau) = 17.8\%$ a total efficiency for tau decays of $\varepsilon_\mu^\tau = 0.0175$ is obtained. The efficiency for the dominant CC reaction is reduced to $\varepsilon_\mu^{CC} = 0.067$, corresponding to 33'500 events out of 5×10^5 CC events to be scanned. The efficiency for detecting the reaction $\bar{\nu}_\mu N \to \mu^+ (\bar{D} \to \mu^-) X$ is 0.0069.

Table 5

Efficiences for selecting events with a muon*

Selection	$\tau^- \to \mu^-$	ν_μ CC	$\bar{\nu}_\mu \to \mu^+ + (D^- \to \mu^-)$
μ^- reconstructed	0.73	0.90	0.76
μ tracking	0.90	0.90	0.90
μ^+ "punch through"	0.95	0.95	0.95
$E_\mu < 30$ GeV	0.92	0.75	0.95
P_T (miss) > 0.4 GeV/c	0.87	0.45	0.68
φ (H-miss. p_T) > 90°	0.90	0.31	0.95
observed kink (10 mrad)	0.84	-	0.65
$p_T^{decay} > 0.24$ GeV/c	0.84	-	0.92
ε_{kin}	0.317	0.081	0.238
μ not detected	-	-	0.048
scanning efficiency	0.66	0.91**	0.66
detector efficiency	0.92	0.92	0.92
beam efficiency***	1.00	1.00	1.00
$BR(\tau^- \to \mu^-)$	0.178		
N_τ/N_μ	0.51		
ε_μ	0.0175	0.067	0.0069

* The efficiencies quoted are multiplicative. They always refer to the sample of events accepted by the preceding cuts.

** Tracking back efficiency.

*** Following a redesign of the neutrino beam, the ν_μ rate has been increased by 17%. We therefore put the beam efficiency to 1.0

NC-Sample Selection

In this sample events without a muon candidate and with at least one well reconstructed negative hadron are selected. Most of these are due to NC interactions and further reduction is obtained using the kinematical differences between these reactions and ν_τ interactions:

a) The hadron energy (figure 21) and the total unbalanced transverse momentum is larger in NC events (figure 22).
b) The angle φ, in the transverse plane, between the h^- and the rest of the hadronic shower is on average larger for ν_τ events (figure 23).

As a result, the following criteria are applied:

1) One negative hadron does not interact before the calorimeter and traverses the front and back face of a single triangle of the hexagonal magnet to ensure good charge determination.
2) Its measured energy lies between 2.5 and 10 GeV. These limits are justified by the performance of the calorimeter and of the air core magnet.
3) The missing transverse momentum p_T^{miss}, is < 2 GeV/c.
4) The angle φ is > 50°.

As for the muon channel, the visibility cuts on the decay vertex scanning and other efficiencies are applied.

The effect of this selection on the $\tau^- \to h^-$ and NC sample is summarised in Table 6. A total of 6.4% of the muonless events have to be scanned. In addition, CC events for which the muon was not detected (10%) have to be scanned bringing the total sample of muonless events to be scanned to ~ 13'000.

Selection of $\tau^- \to \pi^+ \pi^- \pi^-$ (n π^0) ν_τ decays

This decay mode with a branching ratio of 13.8% will also appear in the NC sample. Selecting events which have two negative hadrons with energies in the range $1 < E_h < 10$ GeV and imposing $p_T^{vis} < 2$ GeV/c for both of them, we find a kinematical efficiency of 21%. The total efficiency for τ detection is thus improved by ~ 25%, from 0.041 to 0.050.

The background situation, however, is not so satisfactory. There are no white kinks due to elastic scattering, the contribution of coherent $A_1^- \to \pi^+ \pi^- \pi^-$ production is small, and $K^- \to \pi^+ \pi^- \pi^-$ decays can be eliminated by a modest p_T cut on either of the two measured π^-. However, the background due to the decay $D^- \to h^+ h^- h^-$ (n π^0) is the dominant source. We expect a background of 0.59 events from single charm production (by $\overline{\nu}_\mu$ and $\overline{\nu}_e$) and < 0.12 from A_1 decays, hence in total ≤ 0.71 background events for 5×10^5 ν_μ CC events.

Table 6
Selection efficiency of $\tau^- \rightarrow h^- + X^\circ$

Selection	$\tau^- \rightarrow h^-$	NCυ_μ	$\bar{\nu}_\mu \rightarrow \mu^+ (D^- \rightarrow h^-)$
non-interacting π^-	0.92	0.92	0.92
magnet acceptance	0.85	0.85	0.85
tracking through magnet	0.90	0.90	0.90
charge measured	0.93	0.93	0.93
$2.5 < E_\pi < 10$ GeV	0.38	0.34	0.46
$p_T^{vis} < 2$ GeV/c	0.95	0.62	0.95
φ (π-hadrons) > 50°	0.91	0.58	0.91§
$\theta_{decay} > 10$ mrad	0.86	-	0.81
p_T (decay) > 0.24 GeV/c	0.86	-	0.90
μ^+ "punch through"	0.95	0.95	0.95
ε_{kin}	0.15	0.076	0.179
μ^+ not detected	-	-	0.067
scanning efficiency	0.66	0.91*	0.66
detector efficiency	0.92	0.92	0.92
beam efficiency**	1.00	1.00	1.00
BR ($\tau^- \rightarrow h^-$)	0.50		
N_τ/N_μ	0.51		
ε_h	0.023	0.064	0.0073

The acceptance criteria for $\tau^- \rightarrow 3\pi\nu_\tau$ decays have a large overlap with those for $\tau^- \rightarrow h^- (n\pi^\circ)\nu_\tau$. The sample of NC events to be scanned in addition increases by 7% only. Given the low efficiency and relatively high background it is unlikely that the channel $\tau^- \rightarrow \pi^+ \pi^- \pi^- \nu_\tau$ would contribute in a significant manner to improve the limits on the mixing angle. We consider this decay mode valuable however, since it allows important and independent checks of the background sources.

V.2. Emulsion scanning

Muon or charged hadron tracks adequate for extrapolation to the changeable emulsion sheets (see III.1) must fulfill the following criteria:

** see remark(***) in Table 5
* tracking back efficiency

- the angle with respect to the beam direction is larger than 50 mrad to discriminate against beam muon background;
- this angle is smaller than 250 mrad for easy recognition and track following in the emulsion stacks;
- the momentum is larger than 1.5 GeV/c to limit the effect of multiple scattering.

On the average, there are about two such tracks per event and about 9% of the events have no such track and will not be scanned.

With the reconstruction accuracy (see "tracking system III.2 and III.3), most of the time, the track will be in the predicted field of view of the microscope (300 μm × 300 μm) on the changeable sheet. In this field only $\lesssim 0.5$ muon tracks will be present which can be rejected on the basis of the angular measurement. The higher precision ($\sigma_x \sim 1$ μm and $\sigma(\theta) \sim 1$ mrad) of the track in the changeable sheet permits sharper tolerances on the following of the tracks into the bulk emulsion. One special sheet is mounted permanently on the bulk emulsion. The search can then be continued in a square of 10×10 μm^2 and with better angle tolerance, which again removes background to a negligible level in spite of the long exposure time of this emulsion. Using a computer operated microscope stage, the time needed to follow back the track to the primary vertex is typically 15 minutes. The efficiency of the vertex finding is 0.90 [8]. All forward going tracks are then followed over a maximum distance of 3 mm to search for a kink. To ensure good kink detection efficiency and to reduce background from π^- and K^- decays, the following criteria will be applied:

Kink angle > 10 mrad and decay length > 20 μm,
Transverse momentum relative to the decaying particle > 0.24 GeV/c.

The effect of these cuts on the τ^- and D^- decays is also shown in Tables 5 and 6. This search takes about 5 minutes per event and introduces an additional efficiency factor of 0.92. The fiducial target mass is reduced to 0.88 of the total target mass due to edge effects. These efficiences result in an overall $\varepsilon_{scan} = 0.66$.

V.3. Background Sources

As we are searching for a few, at most 60 ν_τ induced events among 6.5×10^5 ν_μ interactions, background sources have to be explored at the level down to 10^{-7}. Candidates for tau neutrino charged current interactions will be searched for among events without a prompt muon or electron and with a detected decay topology with a high p_t negative muon or hadron. We considered the following sources of background:

(1) Prompt ν_τ production in the primary proton target and in the dump after the decay tunnel.

(2) Background for $\tau^- \rightarrow \mu^-$ decay
  (a) muonic decay of K^-,
  (b) large angle muon scattering near the vertex,
  (c) muonic one-prong decay of charmed particles.

(3) Background for $\tau^- \rightarrow$ hadron$^-$ (n π^0) decay

(a) one-prong decay of strange particles,

(b) one-prong decay of charmed particles,

(c) single-prong interaction of hadrons without visible recoil, blob or Auger electron.

(1) Prompt ν_τ Production in the Primary Proton Target

Direct ν_τ production can occur through the following reactions:

$$p + N \rightarrow D_s + \overline{D} + X$$
$$\hookrightarrow \tau^+ + \nu_\tau,\ \tau^+ \rightarrow \overline{\nu}_\tau + X$$

$$p + N \rightarrow D + \overline{D}_s + X$$
$$\hookrightarrow \tau^- + \overline{\nu}_\tau,\ \tau^- \rightarrow \nu_\tau + X$$

The ν_τ yield at the detector was estimated using the following assumptions : $\sigma(pN \rightarrow D + \overline{D} + X) = 50$ μb/ nucleon, an atomic weight dependence of $A^{0.75}$, $\sigma(D_s) / \sigma(D) = 0.2$. $BR(D_s \rightarrow \tau^+ + \nu_\tau) = 0.02$ and D_s production was parametrized in the same way as D production by

$$\frac{d^2\sigma}{dx_F\, dp_T} = A\,(1-x_F)^n\, e^{-p_T^2}.$$

We assumed for n the values 2.5, 3.5, 4.5 which cover the range of experimental results [19]. Table 7 gives, for the considered n values, the detector acceptance, the mean ν_τ energy and the rate of observable background events per ν_μ induced CC interaction. The contribution of protons escaping the 1 m long Be target and interacting in the beam dump at the end of the decay tunnel has been taken into account. The rate has to be multiplied by the τ branching ratio and the detection efficiency.

Table 7

n	Acceptance	$\bar{E}_{\nu_\tau}$ (GeV)	Background rate / N^{CC}
2.5	7.5×10^{-3}	33.6	1.6×10^{-7}
3.5	5.3×10^{-3}	27.9	0.9×10^{-7}
4.5	4.8×10^{-3}	24.5	0.8×10^{-7}

Assuming n = 2.5 we estimate the following rates:

(a) $\tau^- \rightarrow \mu^-$ decay channel

$$R = N^{CC}_{\nu_\tau} / N^{CC}_{\nu_\mu} \cdot BR(\tau \rightarrow \mu) \cdot \varepsilon(\mu^-) \cdot \varepsilon_{scan} \cdot \varepsilon_{det} \cdot \varepsilon_{beam} \cdot N^{CC}$$

$$R = (1.6 \times 10^{-7}) \cdot (0.178) \cdot (0.317) \cdot (0.66) \cdot (0.92) \cdot (1.00) \cdot N^{CC}$$

$R = 5.4 \times 10^{-9} N^{CC}$

(b) $\tau^- \rightarrow h^-$ decay channel

$R = N_{\nu\tau}^{CC} / N_{\nu\mu}^{CC} \cdot BR(\tau^- \rightarrow h^-) \cdot \varepsilon_h \cdot \varepsilon_{scan} \cdot \varepsilon_{det} \cdot \varepsilon_{beam} \cdot N^{CC}$

$R = (1.6 \times 10^{-7}) \cdot (0.503) \cdot (0.151) \cdot (0.66) \cdot (0.92) \cdot (1.00) \cdot N^{CC}$

$R = 7.3 \times 10^{-9} N^{CC}$.

(2) Background for $\tau^- \rightarrow \mu^-$ Decay

(2a) Muonic Decay of K^-

Since in ν_μ induced CC events, the detection efficiency of the primary muon is very high, the main contribution from this source comes from neutral current events. Muonic decays of π^- will be eliminated by requiring $p_T^{decay} > 0.24$ GeV/c. For K^- the background level is estimated as

$$R = \frac{\sigma(NC)}{\sigma(CC)} \cdot \frac{N(K^-)}{N(NC)} \cdot BR(K^- \rightarrow \mu^-) \cdot \varepsilon(\mu^-) \cdot \varepsilon_{decay} \cdot \varepsilon_{p_T} \cdot \varepsilon_{scan} \cdot \varepsilon_{det} \cdot \varepsilon_{beam} \cdot N^{CC}$$

$R = (0.30) \cdot (0.08) \cdot (0.67) \cdot (0.44) \cdot (6.6 \times 10^{-5}) \cdot (0.09) \cdot (0.66) \cdot (0.92) \cdot (1.00) \cdot N^{CC}$

$R = 2.6 \times 10^{-8} N^{CC}$,

where the fifth term gives the K^- decay probability over 3 mm length from the vertex and the sixth the kinematical efficiency of a decay p_T cut of 0.24 GeV/c.

(2b) Large Angle Muon Scattering

No data exist on the probability for a muon to scatter in the emulsion as a so-called "white" kink, i.e. without additional charged particle, blob or Auger electron. For hadrons, this topology represents typically 1% of the total number of interactions.

An upper limit was obtained from a sample of 60 GeV/c test beam muons crossing the CHARM II detector.

Scaling to the emulsion density, one can estimate $\lambda \geq 10'000$ m for $\Delta\theta > 10$ mrad, and a rate of $\leq 1.7 \times 10^{-8} N^{CC}$.

(2c) Muonic-One-prong Decay of Charmed Particles

The charge of a single charmed particle produced by ν_μ charged current interaction is positive whereas that of a tau lepton would be negative. Therefore, even if the muon coming from the neutrino interaction is missed this is not a background. Charmed antiparticles are negatively charged and

contribute therefore to the background. They can be produced in associated charm production in neutral current neutrino interactions or in $\overline{\nu}_\mu$ charged current interactions.

(i) Associated $c\overline{c}$ production in NC interactions

One-prong decay of D^- among charmed particle pairs may become a background if its associated charmed meson is missed. Referring to a 90% confidence limit for the rate of same sign dimuon production in neutral current neutrino interactions obtained by the CCFR Collaboration [18] ($< 0.8 \times 10^{-4}$) and taking into account a branching ratio of single-prong muonic decay of 16%, the level of this background is estimated as

$$R = \frac{\sigma(NC)}{\sigma(CC)} \cdot \frac{\sigma(c\bar{c})}{\sigma(NC)} \cdot \frac{\sigma(D^-)}{\sigma(c\bar{c})} \cdot BR(D^- \rightarrow \mu^- + \text{neutrals}) \cdot$$

$$\cdot \varepsilon_{kin}(D^-) \cdot \varepsilon_{scan}(D^-) \cdot (1-\varepsilon(c\bar{c})) \cdot \varepsilon_{det} \cdot \varepsilon_{beam} \cdot N^{CC}$$

$$R \leqq (0.30) \cdot (0.8\times10^{-4}) \cdot (0.33) \cdot (0.16) \cdot (0.24) \cdot (0.66) \cdot (0.12) \cdot (0.92) \cdot (1.00) \cdot N^{CC}$$

$$R \leqq 2.2 \times 10^{-8}\, N^{CC},$$

where the third term is the fraction of D^- among all charmed particles and the fourth the branching ratio for $D^- \rightarrow \mu^-$ + neutral decays. The kinematical and scanning efficiency for detecting a D^- decay are given in Tables 5 and 6. The seventh term is the probability of missing the associated partner. In most of the cases the partner of D^- will be a D^+ or a D°. The detection efficiency is estimated at ~ 95% for D^+ and ~ 80% for D°, respectively.

(ii) Single charmed particle production by $\overline{\nu}_\mu$ and $\overline{\nu}_e$.

Single prong muonic decays of negative charmed particles produced in $\overline{\nu}_\mu$ charged current interactions become a background if the primary muon is missed. The observed fraction of $\overline{\nu}_\mu$ CC interactions to ν_μ CC interactions [16] is 2.5×10^{-2} for $E_\nu > 3$ GeV and the fraction of charm production of the total antineutrino cross section is 3% [20]. This background rate is estimated as

$$R = \frac{N(\overline{\nu}_\mu)}{N(\overline{\nu}_\mu)+N(\nu_\mu)} \cdot \frac{\sigma(\overline{\nu}_\mu \rightarrow \mu^+ \bar{c} X)}{\sigma(\overline{\nu}_\mu \rightarrow \mu^+ X)} \cdot \frac{N(D^-)}{N(\bar{c})} \cdot BR(D^- \rightarrow \mu^- + \text{neutrals}) \cdot$$

$$\cdot \varepsilon_{kin}(D^-) \cdot \varepsilon_{miss}(\mu^+) \cdot \varepsilon_{scan}(D^-) \cdot \varepsilon_{det} \cdot \varepsilon_{beam} \cdot N^{CC}$$

$$R = (0.025) \cdot (0.03) \cdot (0.33) \cdot (0.16) \cdot (0.24) \cdot (0.048) \cdot (0.66) \cdot (0.92) \cdot (1.00) \cdot N^{CC}$$

$$R = 2.59 \times 10^{-7}\, N^{CC};$$

the probability to miss the μ^+ is given in Table 5. For the same reaction produced by the $\overline{\nu}_e$ component of the beam we assumed a probability to miss the e^+ from the $\overline{\nu}_e$CC interaction of 50% and obtain a background of

$$R = 2.0 \times 10^{-7}\, N^{CC}.$$

These background estimates are summarised in Table 8. For $N^{CC} = 5 \times 10^5$ we expect less than 0.27 background events for $\tau^- \to \mu^-$ decays.

Table 8
Summary of background for the reaction
$\nu_\tau N \to (\tau^- \to \mu^-) X$

Background	Rate / N^{CC}
prompt ν_τ	$< 0.5 \times 10^{-8}$
$K^- \to \mu^-$ decay	$< 2.6 \times 10^{-8}$
μ scattering	$< 1.7 \times 10^{-8}$
associated charm in NC	$< 2.2 \times 10^{-8}$
single charm in $\bar{\nu}_\mu$ CC	26×10^{-8}
single charm in $\bar{\nu}_e$ CC	20×10^{-8}
total	$\leq 53 \times 10^{-8}$

(3) Background for $\tau^- \to$ Negative Hadron + Neutrals

Most of the previous considerations apply here as well.

(3a) One-prong Decay of Strange Particles

Applying a p_T cut of 0.24 GeV/c eliminates all hyperon and kaon decays at the level of 10^{-8} N^{CC}.

(3b) One-prong Decay of Charmed Particles

Single-prong decays of negative charmed particles produced either in NC interactions or in $\bar{\nu}_\mu$ or $\bar{\nu}_e$ CC interactions can contribute to the background. Following the previous discussion they are estimated as follows:

(i) associated charm production in NC interactions

$$R = \frac{\sigma(NC)}{\sigma(CC)} \cdot \frac{\sigma(c\bar{c})}{\sigma(NC)} \cdot \frac{\sigma(D^-)}{\sigma(c\bar{c})} \cdot BR(D^- \to \text{one negative hadron + neutrals}) \cdot$$
$$\cdot \varepsilon_{kin}(D^-) \cdot \varepsilon_{scan}(D^-) \cdot (1-\varepsilon(c\bar{c})) \cdot \varepsilon_{det} \cdot \varepsilon_{beam} \cdot N^{CC}.$$

$$R = (0.30) \cdot (0.8 \times 10^{-4}) \cdot (0.33) \cdot (0.20) \cdot (0.18) \cdot (0.66) \cdot (0.12) \cdot (0.92) \cdot (1.00) \cdot N^{CC}$$

$$R = 2.1 \times 10^{-8} N^{CC}.$$

(ii) Single charmed particle production by $\bar{\nu}_\mu$ and $\bar{\nu}_e$ CC interactions

Single hadronic prong decays of negative charmed particles produced by $\bar{\nu}_\mu$ and $\bar{\nu}_e$ CC interactions can contribute to the background if the primary positive muon or the e^+ are missed. We estimate the level of this background following the previous discussion.

$$R = \frac{N(\bar{\nu}_\mu)}{N(\nu_\mu)} \cdot \frac{\sigma(\bar{\nu}_\mu \to \mu^+ \bar{c} X)}{\sigma(\bar{\nu}_\mu \to \mu^+ X)} \cdot \frac{N(D^-)}{N(c\bar{c})} \cdot BR(D^- \to \text{one negative hadron + neutrals}) \cdot$$

$$\cdot \varepsilon_{kin}(D^-) \cdot \varepsilon_{miss}(\mu^+) \cdot \varepsilon_{scan}(D^-) \cdot \varepsilon_{det} \cdot \varepsilon_{beam} \cdot N^{CC}$$

$$R = (0.025) \cdot (0.03) \cdot (0.33) \cdot (0.2) \cdot (0.18) \cdot (0.067) \cdot (0.66) \cdot (0.92) \cdot (1.00) \cdot N^{CC}$$

$$R = 3.6 \times 10^{-7}\, N^{CC}.$$

The probability to miss the μ^+ is given in Table 6. The contribution due to the $\bar{\nu}_e$ component of the beam is estimated as

$$R = \frac{N(\bar{\nu}_e)}{N(\nu_e)} \cdot \frac{\sigma(\bar{\nu}_e \to e^+ \bar{c} X)}{\sigma(\bar{\nu}_e \to e^+ X)} \cdot \frac{N(D^-)}{N(c\bar{c})} \cdot BR(D^- \to \text{one negative hadron + neutrals}) \cdot$$

$$\cdot \varepsilon_{kin}(D^-) \cdot \varepsilon_{miss}(e^+) \cdot \varepsilon_{scan}(D^-) \cdot \varepsilon_{det} \cdot \varepsilon_{beam} \cdot N^{CC}$$

$$R = (1.7 \times 10^{-3}) \cdot (0.03) \cdot (0.33) \cdot (0.2) \cdot (0.18) \cdot (0.5) \cdot (0.66) \cdot (0.92) \cdot (1.00) \cdot N^{CC}$$

$$R = 1.8 \times 10^{-7}\, N^{CC},$$

where the probability to miss the primary e^+ is 50%.

(3c) Single-prong Interaction of Secondary Hadrons ("white kink")

A negative secondary hadron from a NC interaction may scatter within 3 mm from the vertex without a visible recoil, blob or Auger electron. This process contributes a background estimated as

$$R = \frac{\sigma(NC)}{\sigma(CC)} \cdot \frac{N(h^-)}{N(NC)} \cdot \frac{3\ mm}{\lambda_{kink}} \cdot \varepsilon_{kin}(h^-) \cdot \varepsilon_{scan} \cdot \varepsilon_{det} \cdot \varepsilon_{beam} \cdot N^{CC}.$$

$$R = (0.3) \cdot (1.26) \cdot (3.75 \times 10^{-5}) \cdot (0.076) \cdot (0.66) \cdot (0.92) \cdot (1.00) \cdot N^{CC}$$

$$R = 6.5 \times 10^{-7}\, N^{CC}.$$

The interaction length λ_{kink} for so-called "white" kink hadron scattering, without visible recoil, blob or Auger electron has been measured recently in an emulsion exposure at KEK. Selecting events with a decay $p_T > 0.24$ GeV/c, $\lambda_{kink} \geq 80$ m was found. This result is based on four events assuming that they are all elastically scattered. In the near future the experiment will be repeated with momentum analysis of the scattered pion. The selection criteria entering in $\varepsilon_{kin}(h^-)$ are summarised in Table 6.

(3d) "White kink" background from coherent $A_1^- \rightarrow \pi^-\pi^\circ\pi^\circ$ production

Based on Monte Carlo simulations using as input experimental pion spectra from ν interactions in BEBC (WA59) we obtained a background of 22×10^{-8}.

These background estimates are summarised in Table 9. For $N^{CC} = 5 \times 10^5$ we expect 0.72 background events for $\tau^- \rightarrow h^-$ decays

All background estimates are based, wherever possible, on presently available data. It is important to note that, except for the prompt ν_τ background the proposed experiment will allow their evaluation by appropriate adaptation, on partial samples, of the event selection criteria.

Table 9

Summary of background for the reaction $\nu_\tau N \rightarrow (\tau^- \rightarrow h^-) X$

Background	Rate / N^{CC}
prompt ν_τ	$\leq 0.6 \times 10^{-8}$
associate charm in NC	2.1×10^{-8}
single charm in $\bar{\nu}_\mu$ CC	36×10^{-8}
single charm in $\bar{\nu}_e$ CC	18×10^{-8}
white kinks	65×10^{-8}
white kinks from $\pi \rightarrow 3\pi$	22×10^{-8}
total	144×10^{-8}

V.4. Sensitivity to $\nu_\mu \leftrightarrow \nu_\tau$ Oscillations

The branching ratios and the efficiencies for the muon, single charged hadron, and $\pi^-\pi^+\pi^-$ decay modes, averaged over the energy spectrum of tau leptons produced, are summarised in Table 10. Also given is the number of events (N_τ) expected from $\nu_\mu \leftrightarrow \nu_\tau$ oscillation with $\Delta m^2 > 40$ eV^2 and $\sin^2 2\theta = 5 \times 10^{-3}$, a value corresponding to the present limit [18] and the background.

Table 10

Efficiency of τ^- detection

Decay mode	Branching ratio (BR)	Efficiency (ε)	N_τ	Background
$\mu^- \bar{\nu}_\mu \nu_\tau$	0.178	0.098	23	0.27
$h^- (n\pi^\circ)\nu_\tau$	0.50	0.046	29	0.72
$\pi^-\pi^+\pi^-(n\pi^\circ)\nu_\tau$	0.138	0.065	12	0.71
ε total		0.0493	64	1.70

In the hypothetical case that all incident ν_μ oscillate into ν_τ we would expect

$$N_\tau\,(\mathrm{max}) = \int \sigma_\tau\, dE_\nu\, (dN_\nu / dE_\nu)$$

events, σ_τ is the cross section for the reaction $\nu_\tau N \rightarrow \tau^- X$. The integrated ν_μ spectrum is

$$N_\mu = \int \sigma_\mu\, dE_\nu\, (dN_\nu / dE_\nu)\,.$$

The flux integrals have been determined by scaling the CHARM II results [21] to the new detector position with the help of a MC simulation [17]. We find $N_\tau / N_\mu = 0.51$. In the limit of large $\Delta m^2_{\mu\tau}$where oscillations are washed out ($\Delta m^2 \gg \frac{L}{E} \cdot 1.27$) the sensitivity for the $\nu_\mu \leftrightarrow \nu_\tau$ mixing parameter $\sin^2 2\theta_{\mu\tau}$ can be estimated as

$$\sin^2 2\theta_{\mu\tau} < \frac{2 \cdot N_\tau\,(\mathrm{observed})}{\varepsilon_{\mathrm{total}} \cdot N_\tau\,(\mathrm{max})}\,.$$

For $N^{CC} = 5 \times 10^5$ we expect 1.70 background events.

In the case of a negative result the expected sensitivity for the mixing angle at the 90% confidence limit will be

$$\sin^2 2\theta_{\mu\tau} < \frac{2 \cdot 3.84}{0.050 \cdot N^{CC}} = 3.1 \times 10^{-4}\,.$$

This is a factor of 16 improvement over the previous limit of E531 of 5×10^{-3} [8] at large Δm^2.

V.5. Further improvements in sensitivities based on vertex kinematics

In the case of observation of a few candidate events additional kinematical information can be extracted from the observed τ track direction. The essential feature of the CHORUS experiment is the precise measurement of trajectories at the neutrino interaction vertex. As described in our original Proposal, the selection of "decay kinks" eliminates most of the ν_μCC and ν_μNC background. The remaining background is mainly due to charm decays following $\overline{\nu}_\mu N$ and $\overline{\nu}_e N$ charged-current interactions where the accompanying μ^+ and e^+ are not identified, as well as to pion "white kink" in ν_μNC interactions.

These background events can be further reduced by considering the transverse angle distributions between the kink parent with the shower jet and with the missing p_T.

Based on simulations we expect that these further selections will improve the signal to background ratio by a factor of up to 5 relative to the Proposal. In the case of a negative search, the $\sin^2 2\theta$ limit at large Δm^2 will be improved to 2.8×10^{-4}. The updated exclusion plot is displayed in figure 1. In the case of positive results, the statistical significance of the measurement will be enhanced by a factor of 30, thereby greatly increasing the discovery potential of CHORUS.

VI. Beam Time Estimate and Schedule

Based on an experimentally determined flux integral [21] scaled to the position of this experiment using a Monte Carlo simulation of the beam and its spectrum (IV.3), we estimated the required number of protons on the target (T9) of the CERN-SPS neutrino facility and found 2.4×10^{19} protons. Continuing the successful double spill operation with 2×10^{13} protons / cycle it would require 1.3×10^{6} cycles or 222 days to obtain 2.4×10^{19} protons. Experience over the years 1987-1990 gives an average efficiency of ~ 50%. The neutrino facility would therefore have to be operated during two years of extended LEP operation for ~ 200 days per year to match the unique possibility to explore this domain of $\nu_\mu \leftrightarrow \nu_\tau$ mixing.

A test run with the rebuilt neutrino beam is scheduled for November 1993.

Data-taking should take place in 1994 and 1995. We plan to exchange one of the four emulsion stacks during the shut down between 1994 and 1995 to start the analysis.

References

[1] See e.g. R. Davis Jr., K. Lande, C.K. Lee, P.Wildenhain, A. Weinberger, T. Daily, B. Cleveland, J. Ullman; Proc. 21st International Cosmic Ray Conf., Adelaide, Australia, in press (1990).

[2] K.S. Hirata et al., Kamiokande II Collaboration; Phys. Rev. Lett. **65** (1990) 1301.

[3] SAGE Collab., A.I. Abazov et al.; Phys. Rev. Lett. **67** (1991) 3332.

[4] GALLEX Collab., P. Anselmann et al.; Phys. Lett. **285B** (1992) 376.

[5] M. Spiro, D. Vignaud; Phys. Lett. **242B** (1990) 279.
J.N. Bahcall, H.A. Bethe, Astrophysics Preprint IASSNS-AST 90/14, Princeton (1990).

[6] H. Harari; Phys. Lett. **216B** (1989) 413.

[7] Letter of intent, CHARM II Collaboration - Ferrara Univ. - IHEP (Zeuthen) - Nagoya Univ. (Japan) - Rome Univ. (Emulsion group), CERN - SPSC/89-46.

[8] N. Ushida et al.; Phys. Rev. Lett. **57** (1986) 2897.

[9] N. Ushida et al.; Nucl. Instr. Methods **224** (1984) 50.
S. Aoki et al.; Nucl. Instr. Methods **B51** (1990) 466.

[10] A. Artamonov et al.; Nucl. Instr. Methods **A300** (1990) 53.
M. Adinolfi et al.; Nucl. Instr. Methods **A311** (1992) 91.

[11] B. Hoffmann, H.E. Roloff, Zeuthen (IHEP), preprint 1990.

[12] D. Acosta et al.; Nucl. Instr. Methods **A294** (1990) 193.
D. Acosta et al.; CERN-PPE/90-172.

[13] CERN/DRDC/90-23, DRDC/P1.

[14] M. Holder et al.; Nucl. Instr. Methods **148** (1978) 235.

[15] K. de Winter et al.,CHARM II Collaboration; Nucl. Instr. Methods **A278** (1989) 670.

[16] D. Geiregat et al., CHARM II Collaboration; Phys. Lett. **232B** (1989) 539.

[17] 'G-Beam' is a new Monte Carlo Programme to simulate the neutrino beam. Ch. Foos, CHARM II Collaboration, Internal Note (1989), unpublished.

[18] N. Ushida et al. (531); Phys. Lett. **206B** (1988) 375.

[19] M.E. Duffy et al. (E613); Phys. Rev. **D38** (1988) 2032.
M. Aguilar-Benitez et al. (LEBC); Z. Phys. **C40** (1988) 321.
J. Dorenbosch et al. (CHARM); Z. Phys. **C40** (1988) 497.

[20] H. Abramowicz et al. (CDHS); Z. Phys. **C15** (1982) 497.

[21] D. Geiregat et al., CHARM II Collaboration; Phys. Lett. **247B** (1990) 131. The flux integral has been determined from inclusive ν_μ interactions (NC and CC) with an uncertainty of $\pm 4.7\%$.

[22] CCFR Collaboration, W.H. Smith et al.; Nucl. Phys. B (Proc. Suppl.) **31** (1993) 262.

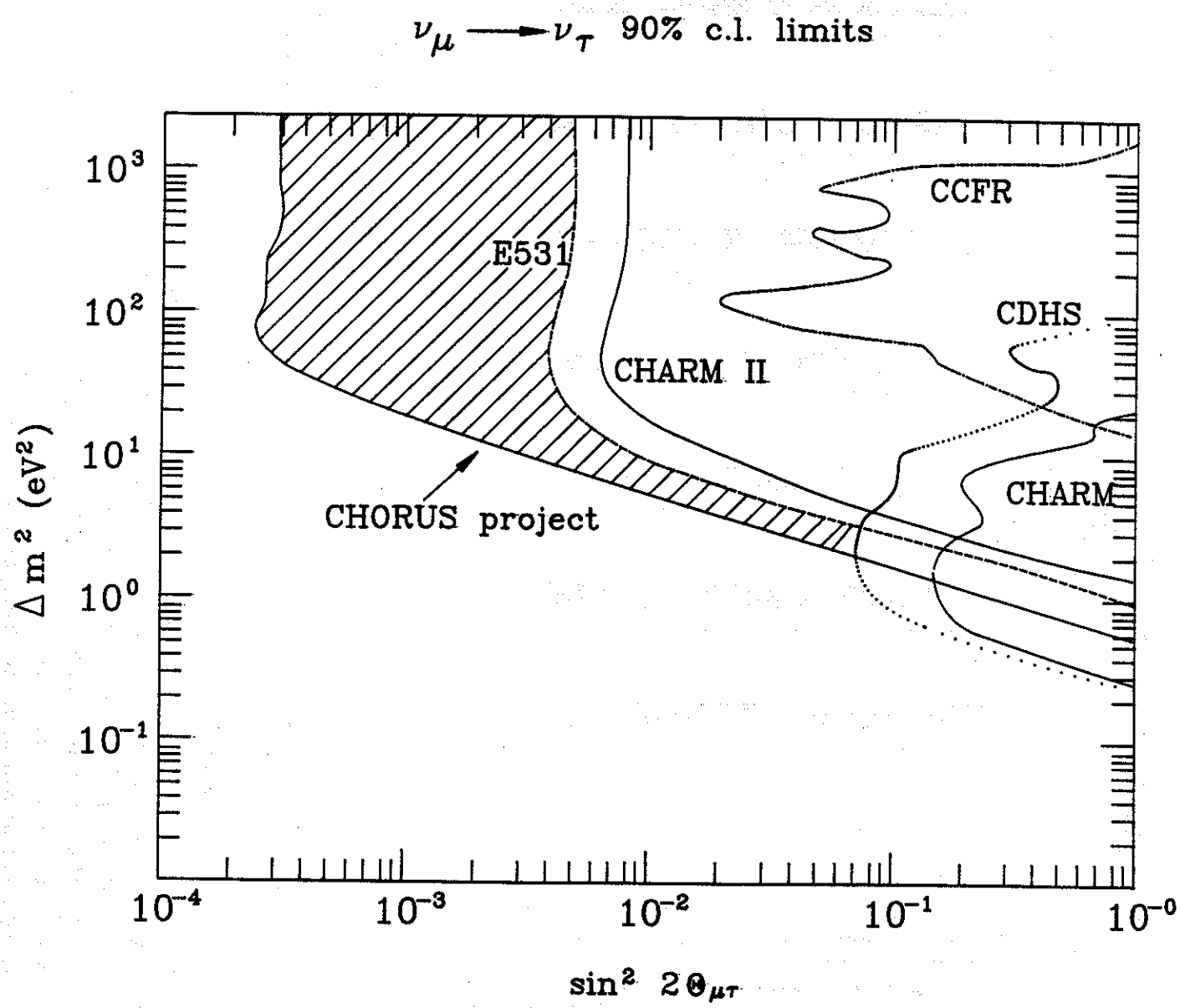

Figure 1

Domains of $(\Delta m)^2$ and $\sin^2 2\Theta_{\mu\tau}$ explored by previous experiments and to be explored by the CHORUS experiment.

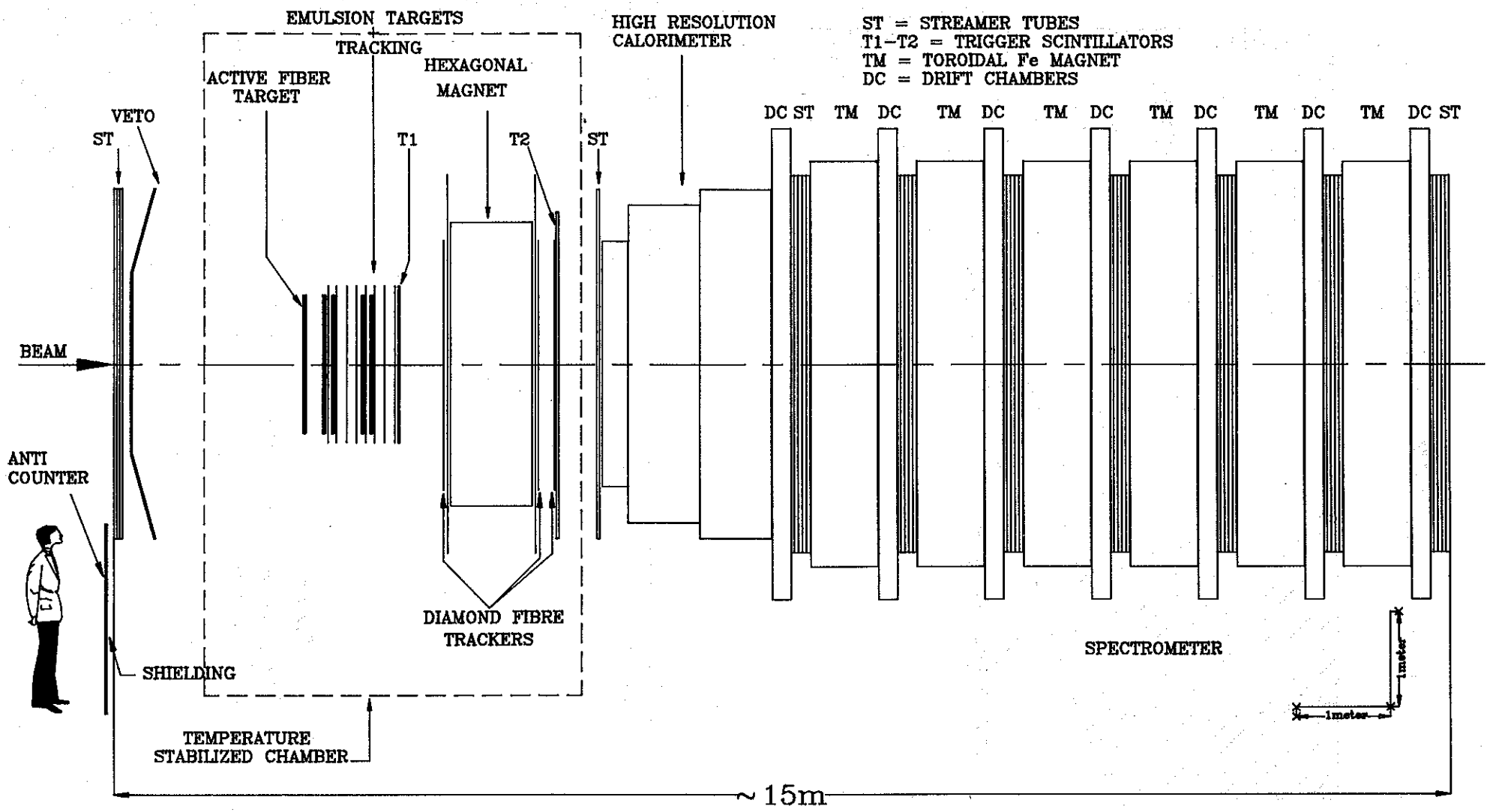

Figure 2

Experimental set-up with 4 emulsion targets and a scintillating fiber target. Scintillating fiber arrays locate the impact point of the decay track. A hexagonal magnet determines its charge and momentum. A high resolution calorimeter determines the direction and the energy of the hadron shower. The muon spectrometer identifies muons and determines their charge and momentum. T1 and T2 and veto are scintillation hodoscopes for triggering.

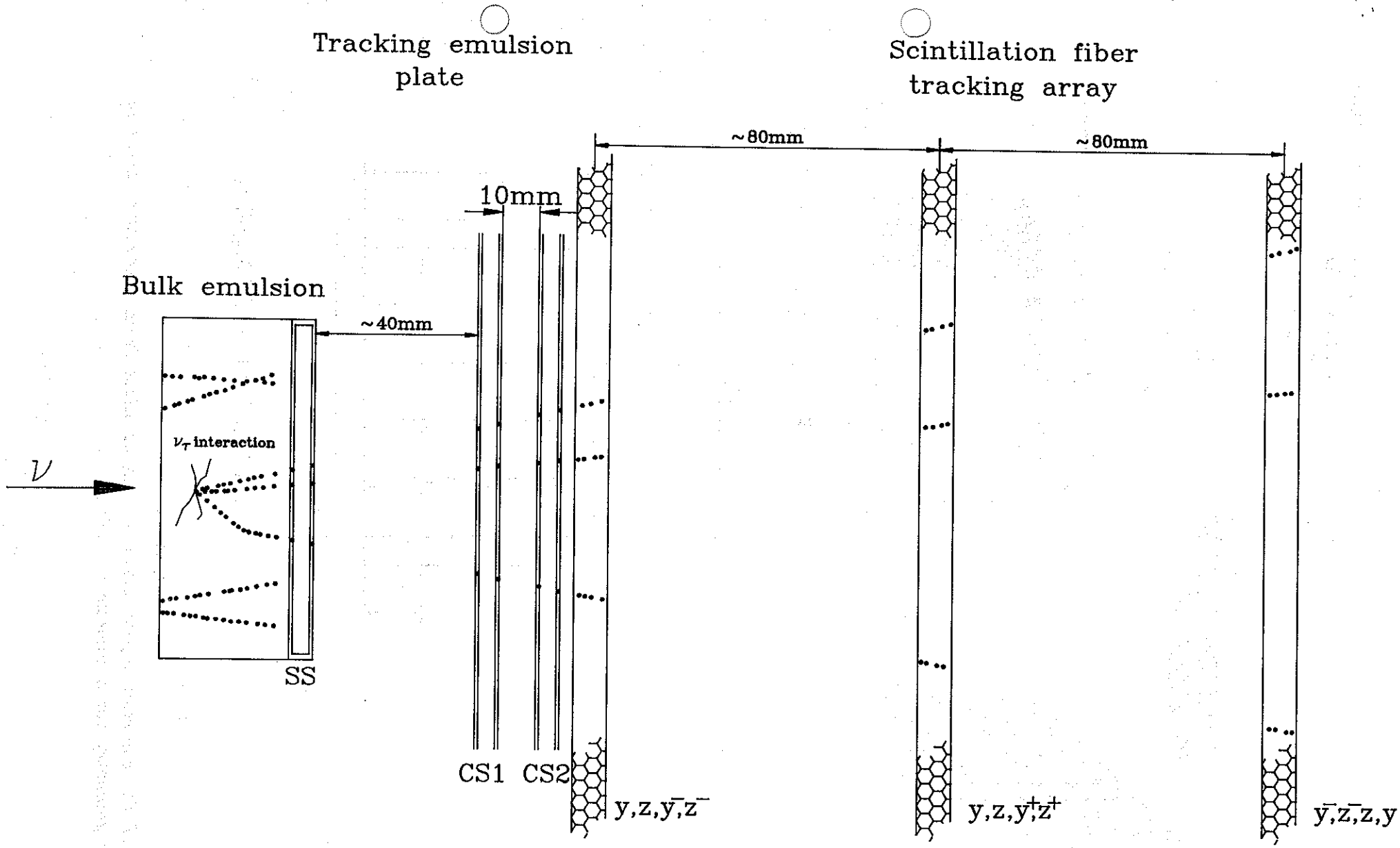

Figure 3

Tracking in the target region of the CHORUS Detector

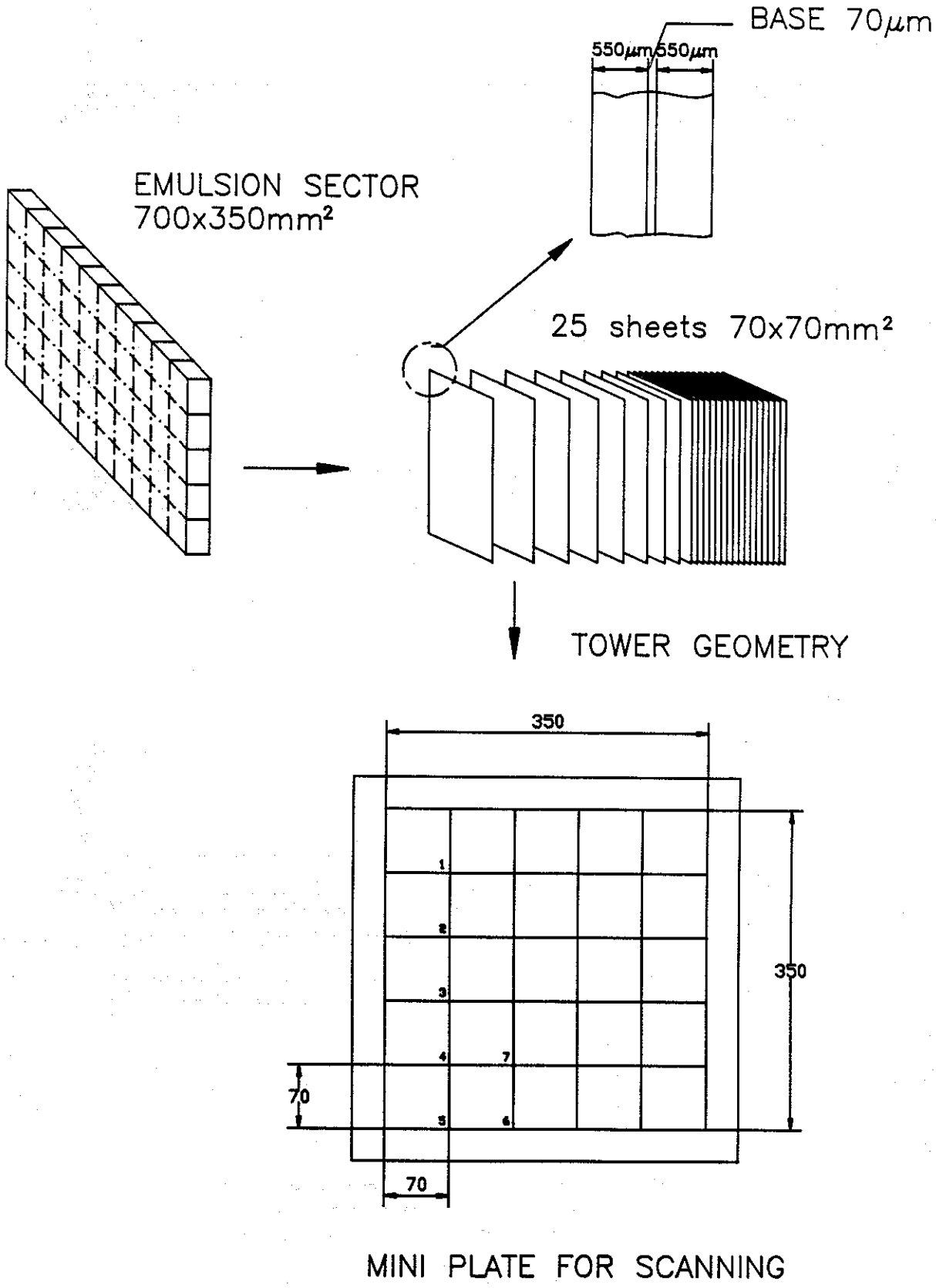

Figure 4

Slicing of the emulsion layers and mounting of slices from successive layers in a tower geometry for automatic scanning.

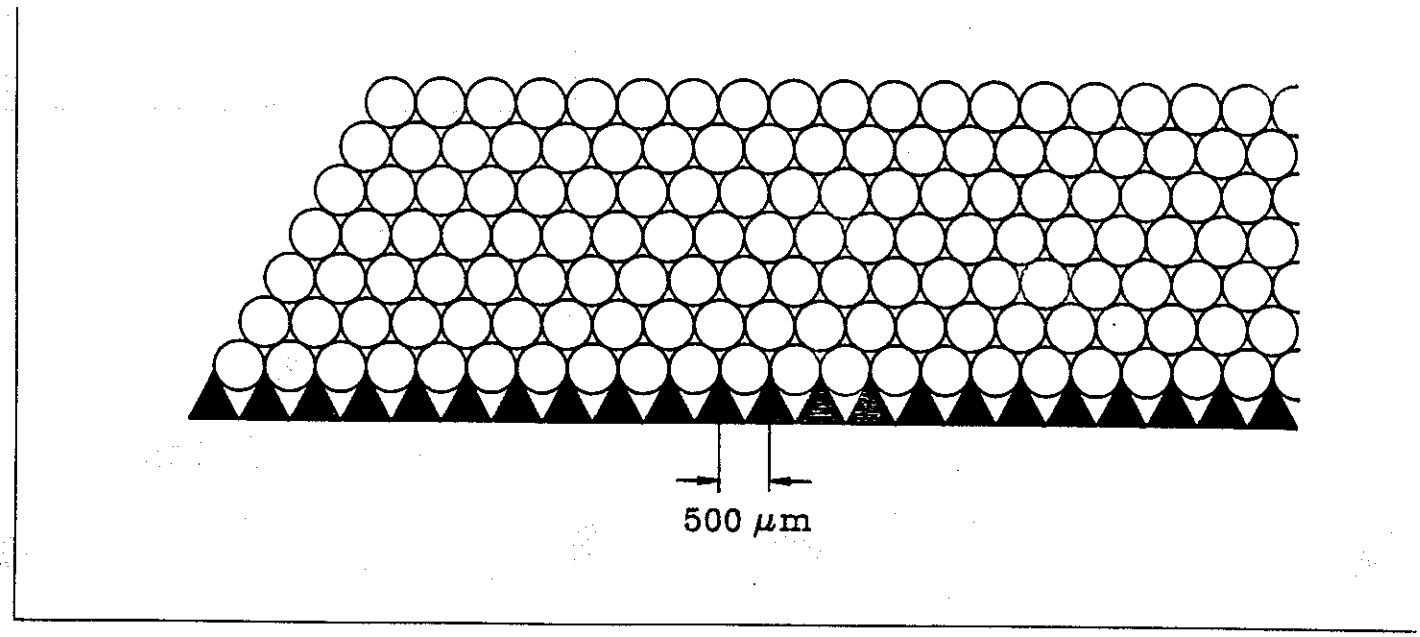

Figure 5

A ribbon of seven staggered scintillating fiber layers.

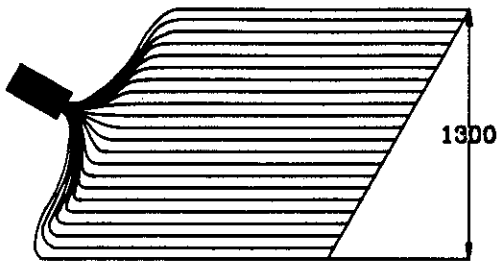

active area ~1m^2
thickness 3.2mm
fibre diameter 0.5mm

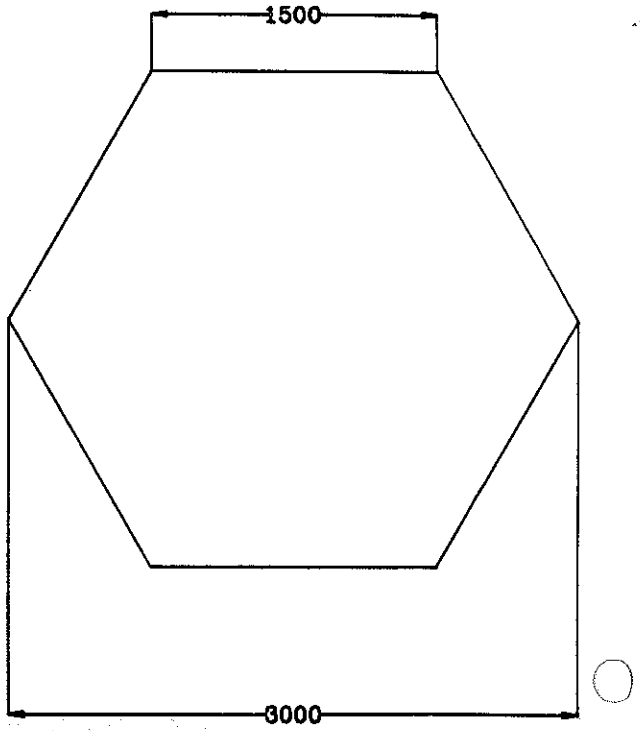

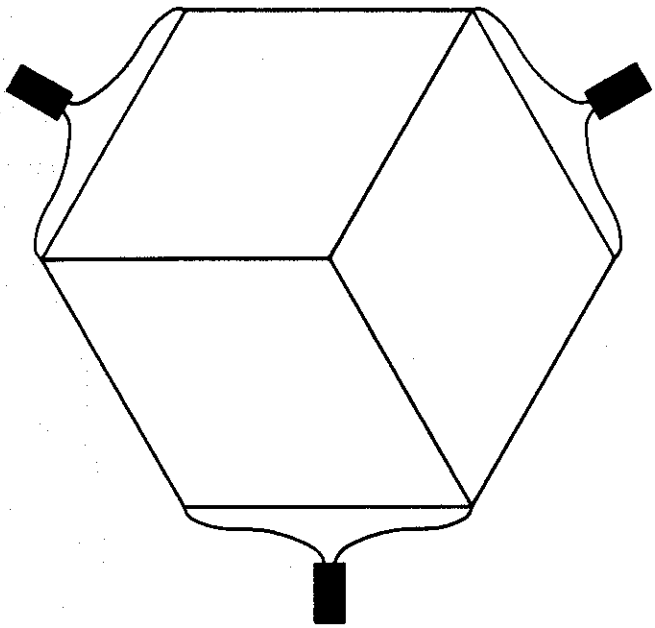

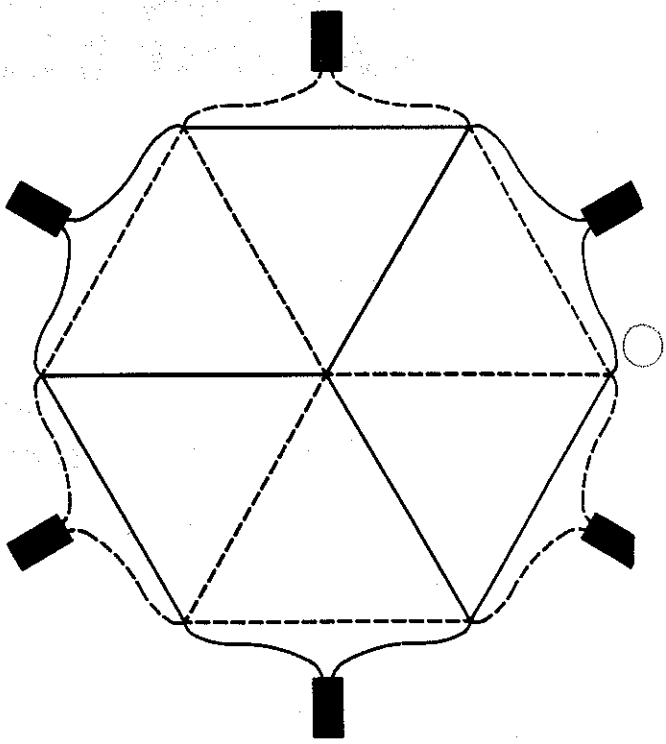

Figure 6

Diamond-shaped trackers in front and behind the hexagonal magnet.

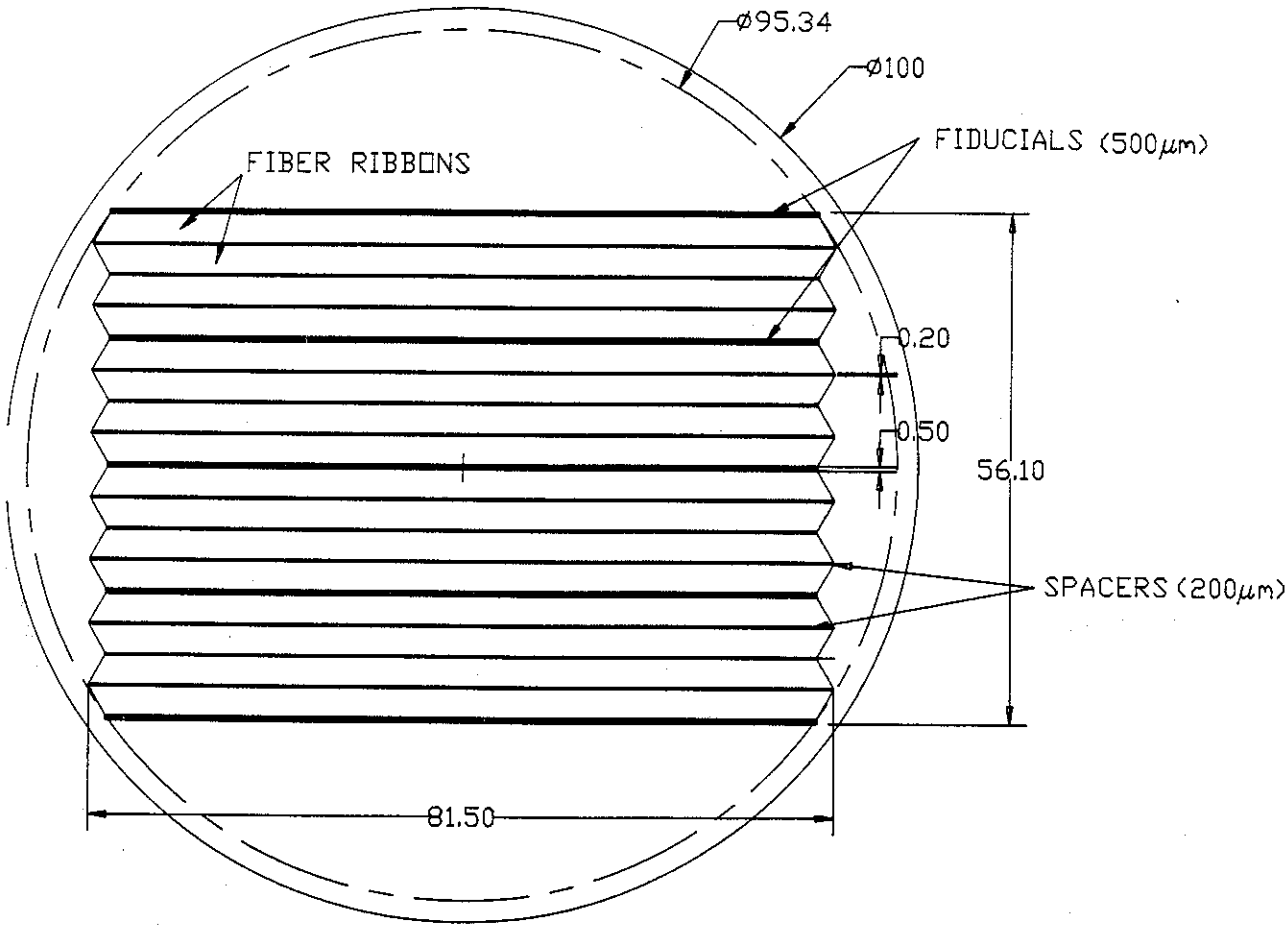

Figure 7

16 fiber ribbons from the trackers bundled onto the photocathode of the first image intensifier. The ribbons are 3.2 mm thick and separated by spacers of 0.20 mm thickness. There are five spacers of 0.50 mm thickness each containing 9 fiducial fibers.

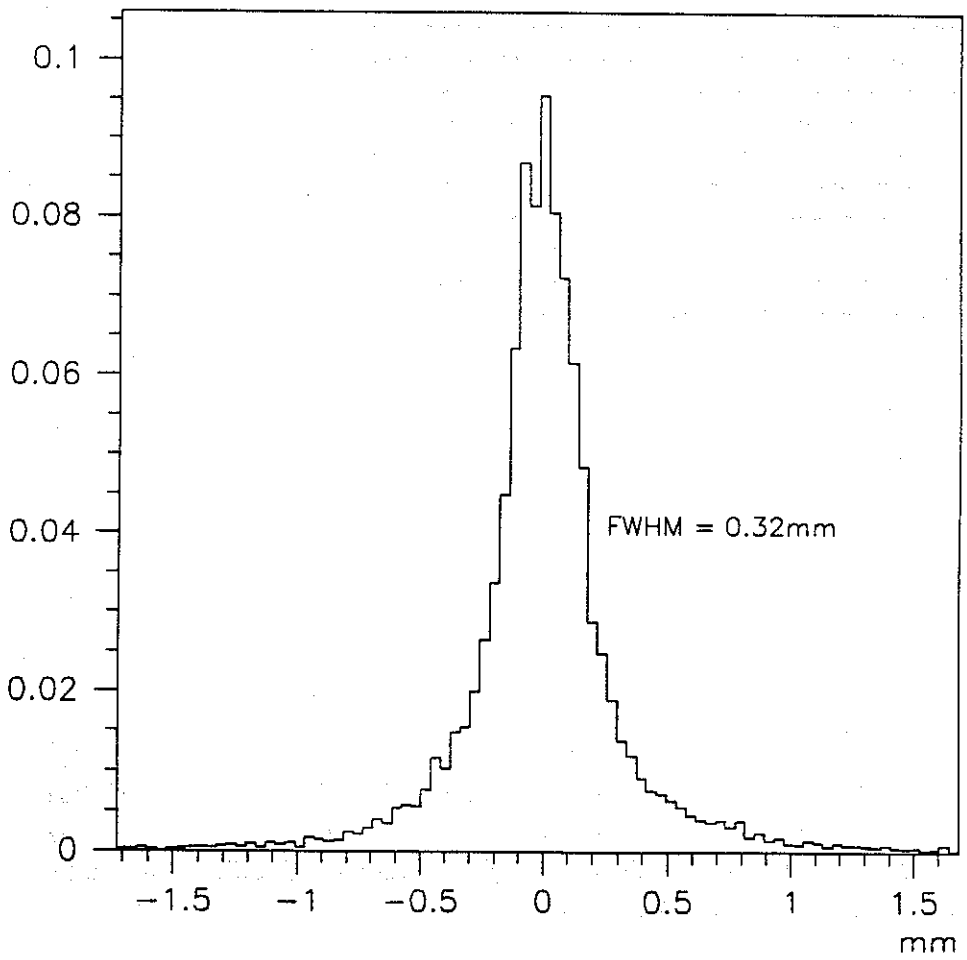

Figure 8

Result of tests of fiber ribbons in a pion beam.

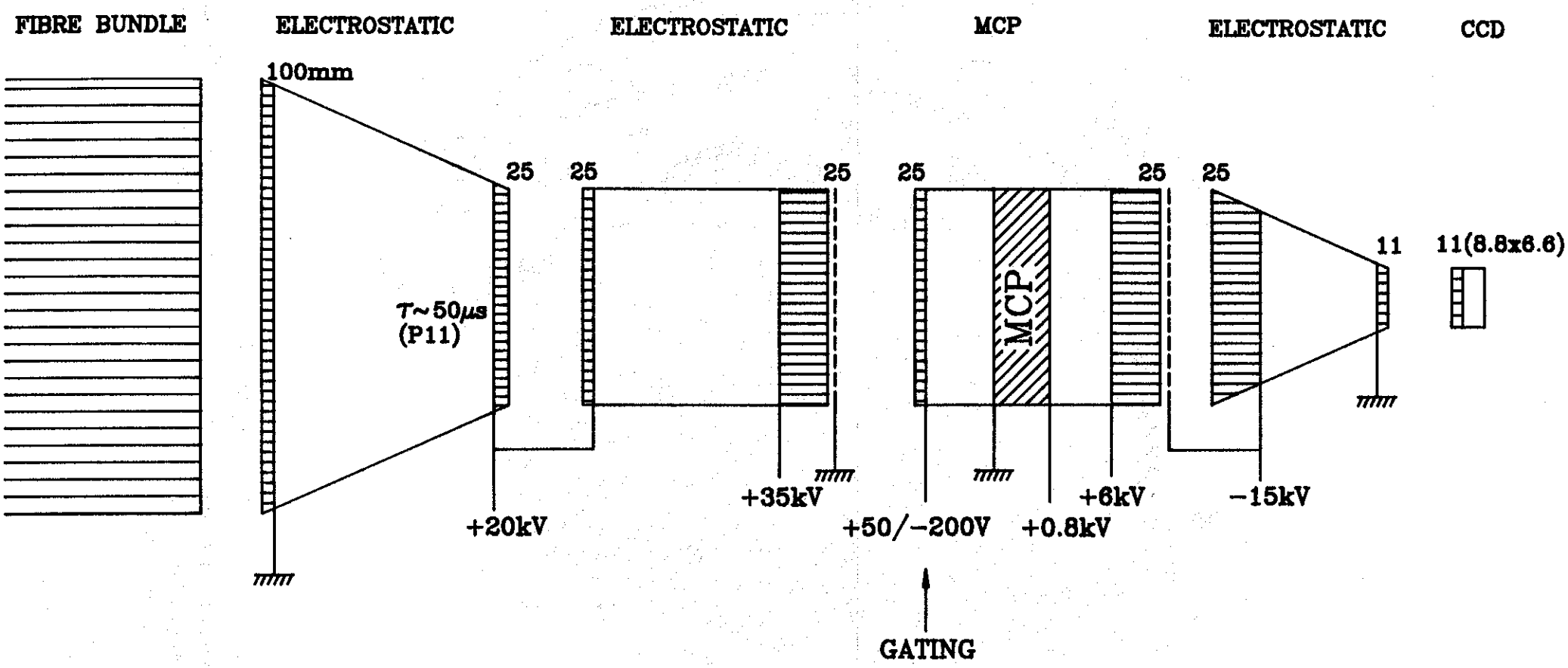

Figure 9

Chain of image intensifiers read out by a CCD. The mircrochannel plate is gated. The total demagnification is 9.1, providing 6 pixels per fiber.

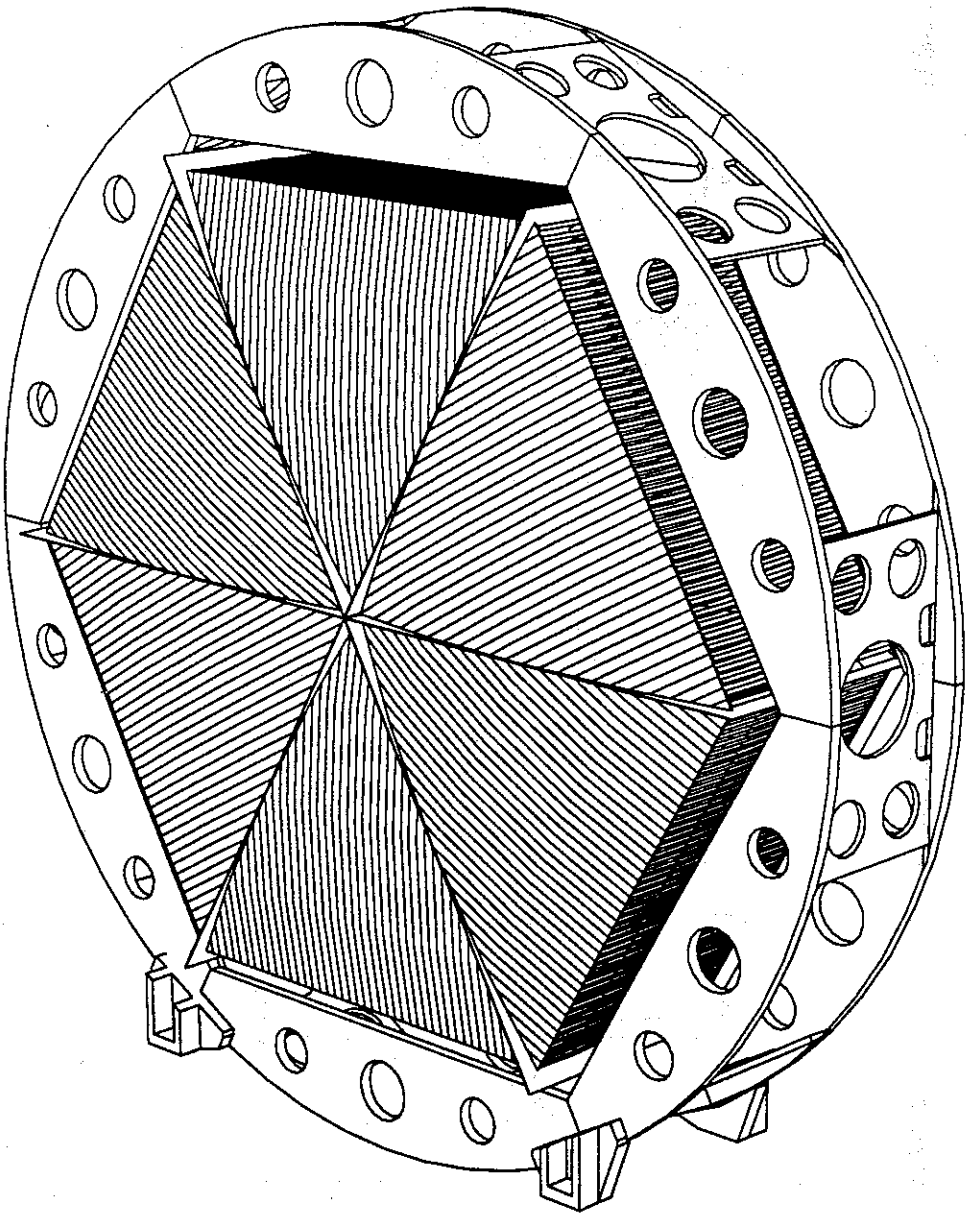

Figure 10

Hexagonal magnet. The magnetic field is oriented vertically to the strips. The field strength inside the sectors is 0.12 T. The magnet is pulsed during the neutrino spills.

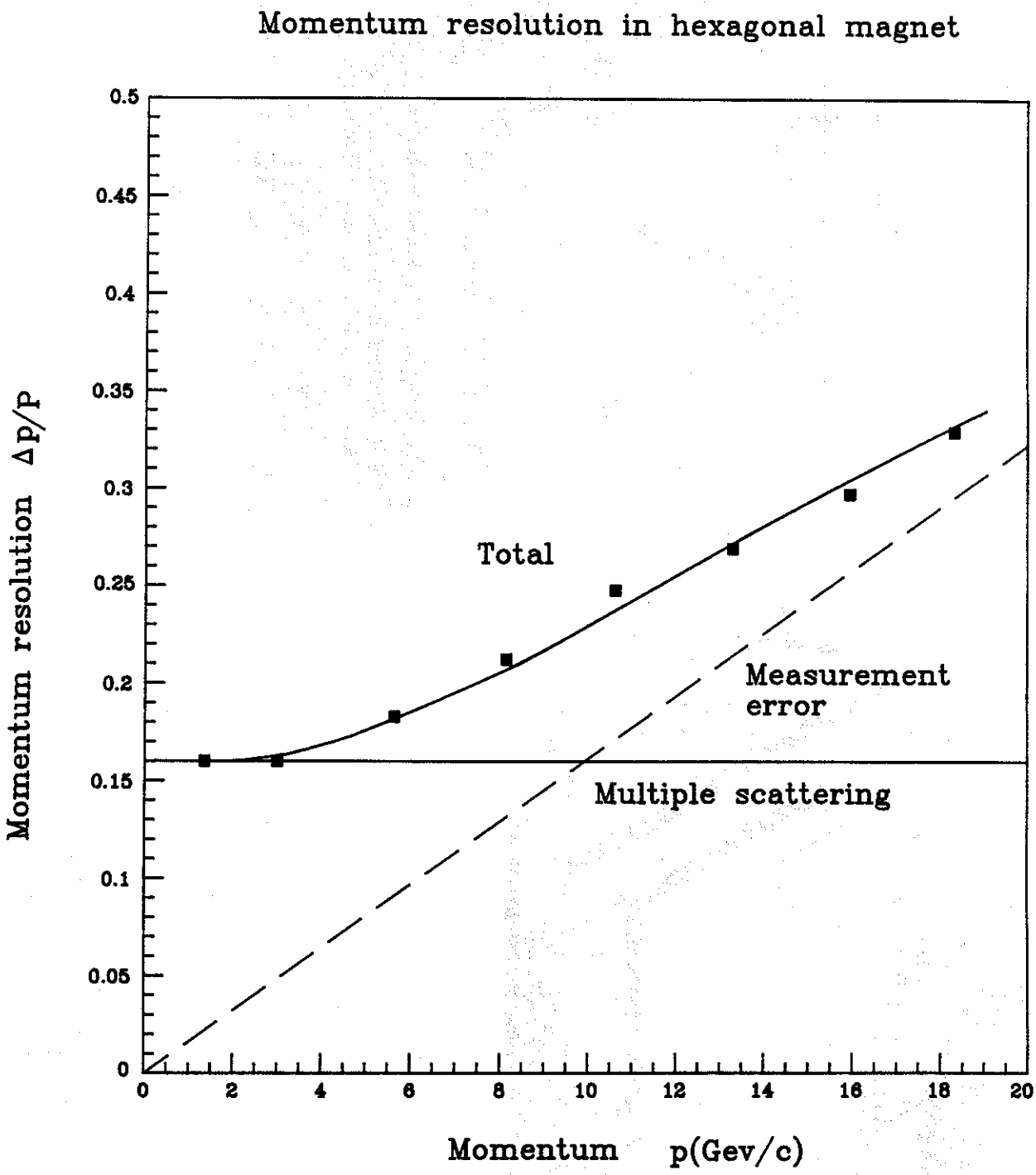

Figure 11

Momentum resolution as a function of momentum obtained from the deflection in the hexagonal magnet and measurements by the diamond trackers.

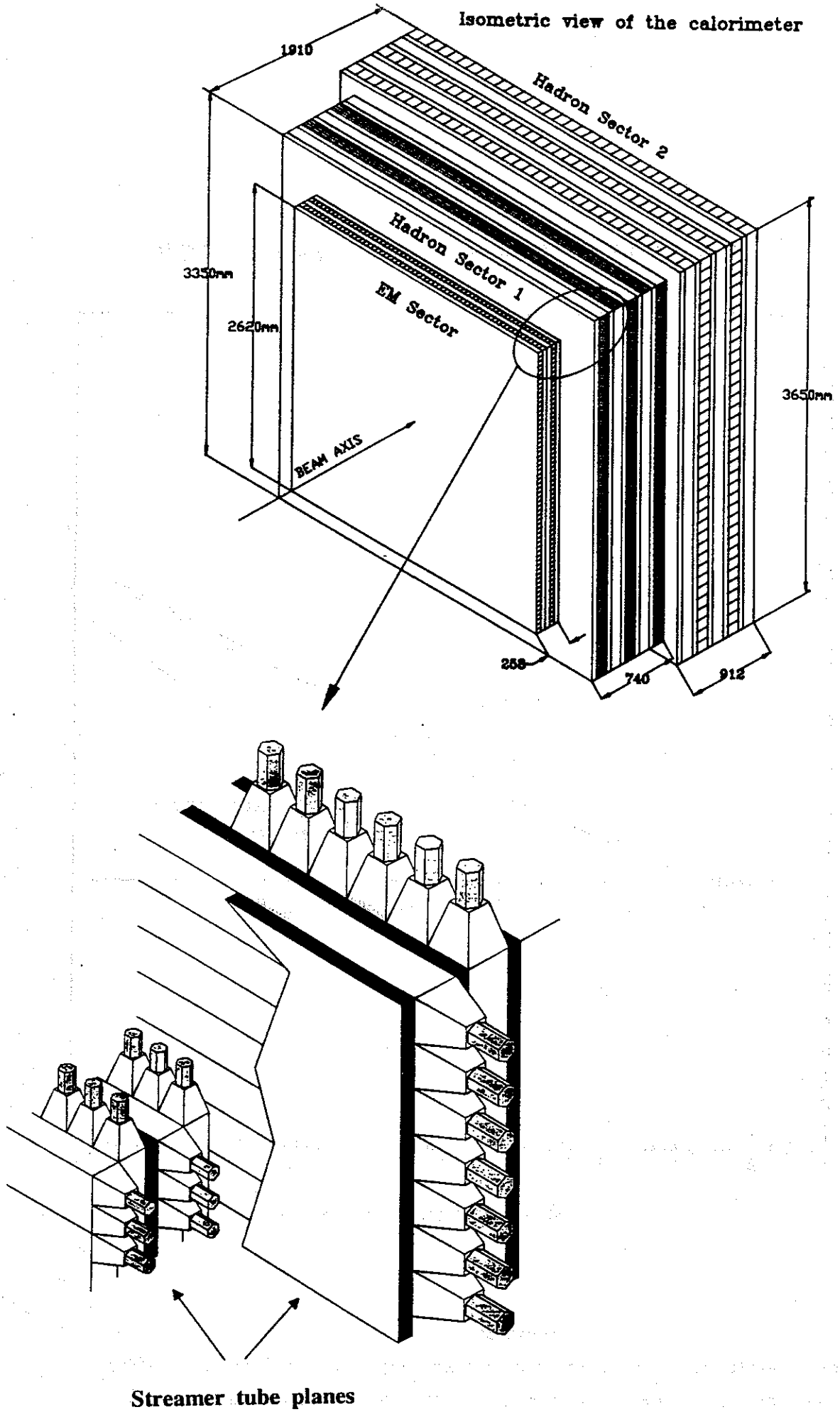

Figure 12(a)

Isometric view of the high resolution calorimeter.

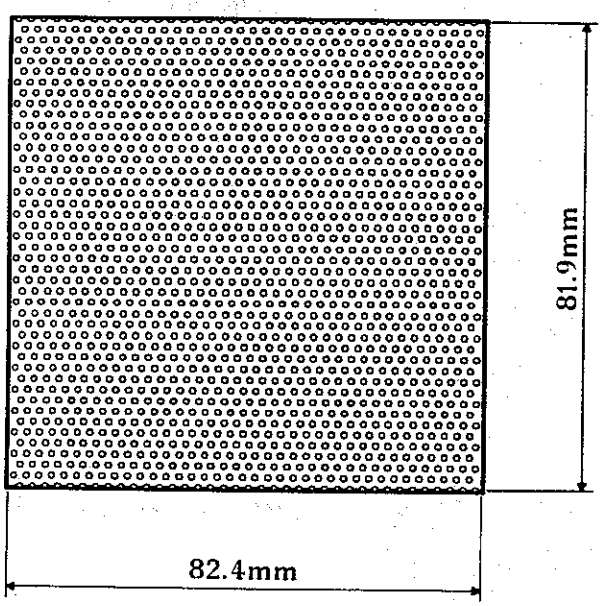

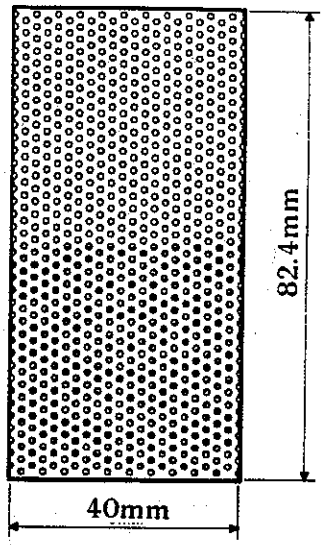

HAD1 module: 82.4 x 81.9 mm^2
43 layers
1554 fibers
total fiber surface: 12.20 cm^2

EM module: 40 x 82.4 mm^2
21 HAD1 layers
740 fibers
EM module surface: 40 x 41.2 mm^2
total fiber surface: 11.62 cm^2

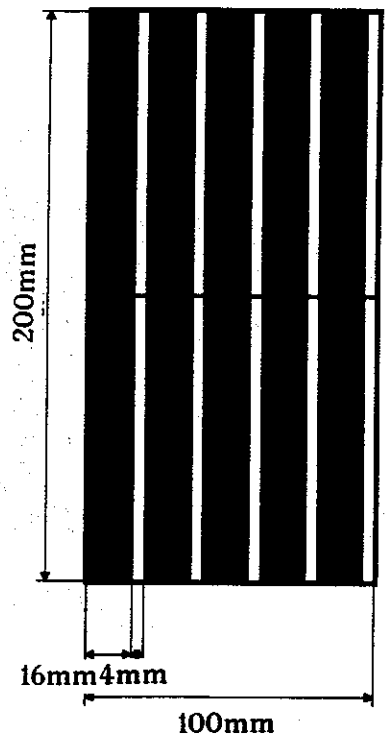

HAD2 module: 100 x 200 mm^2
10 scintillator strips

Figure 12(b)

Fiber and strip structure of HAD1, EM and HAD2.

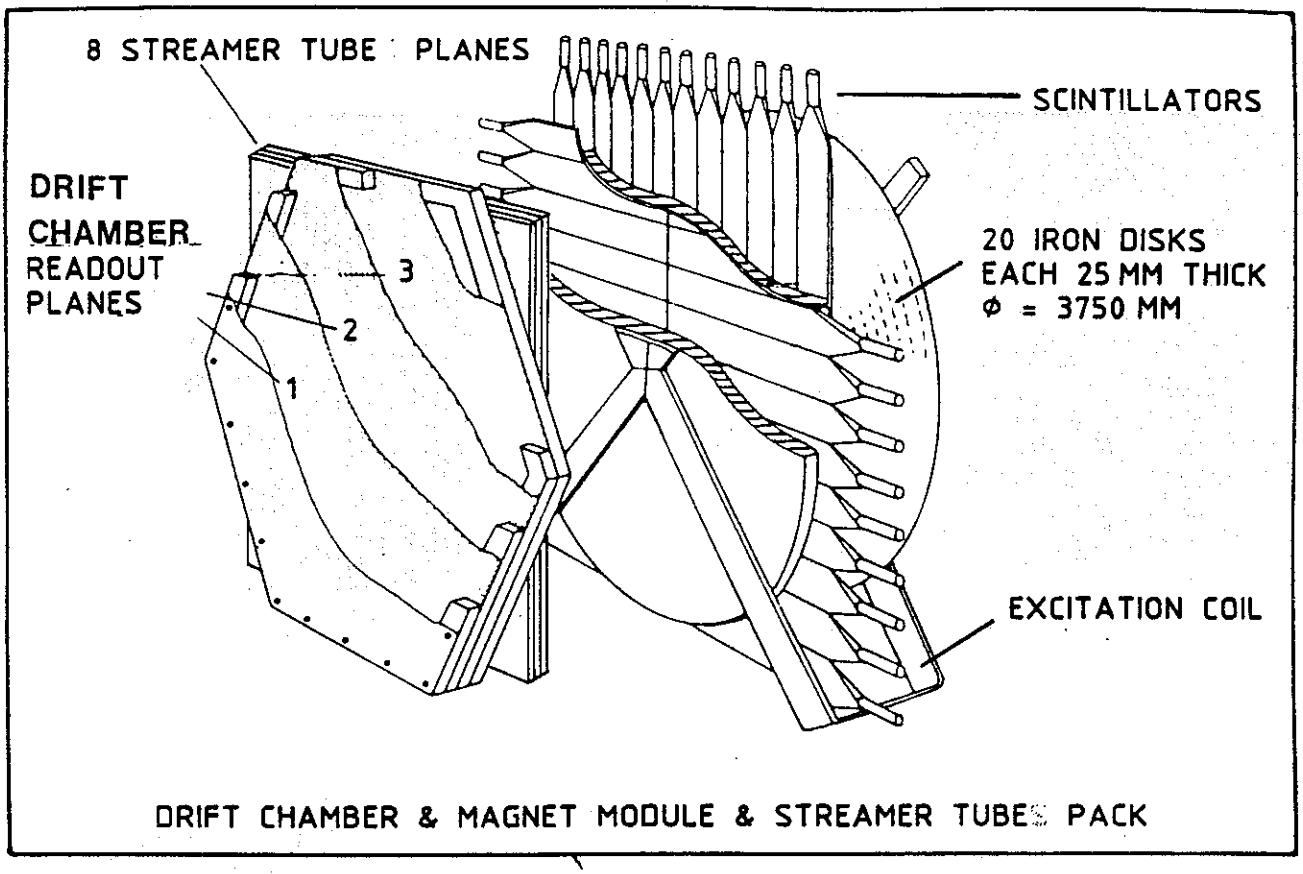

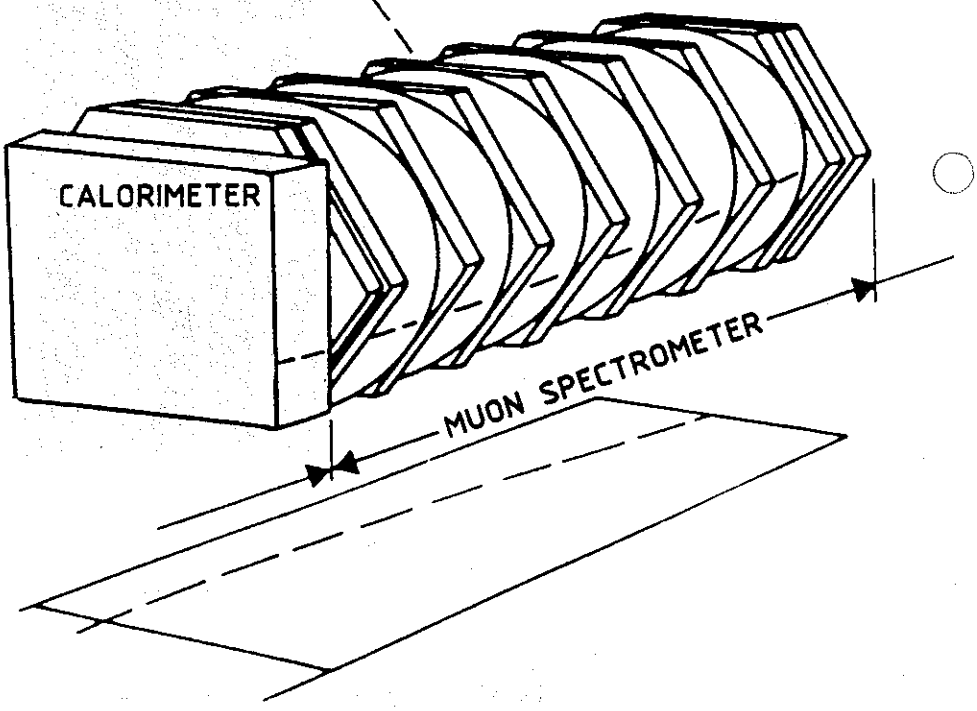

Figure 13

Muon spectrometer with details of the tracking and of the scintillator hodoscopes.

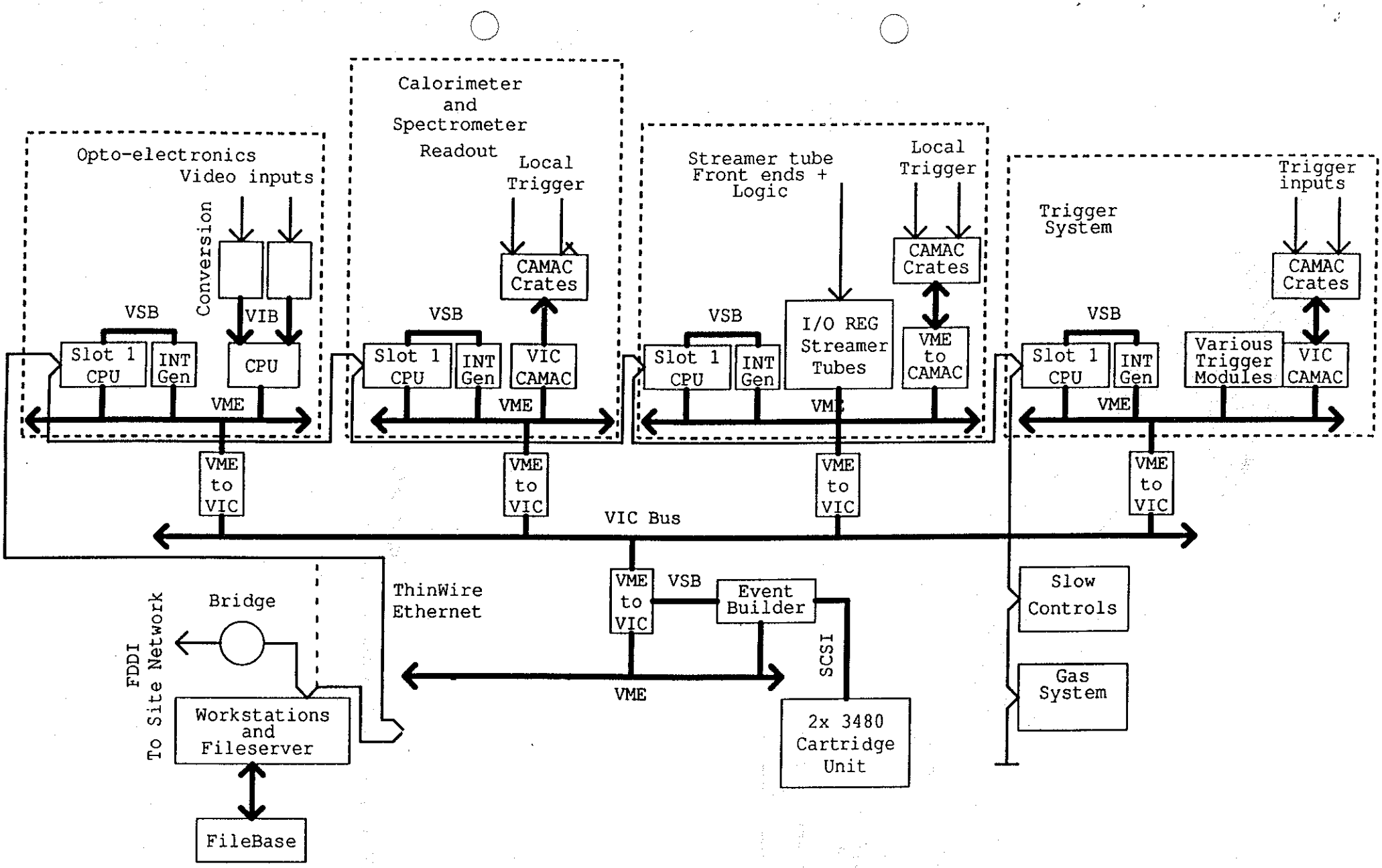

Figure 14

Data acquisition system.

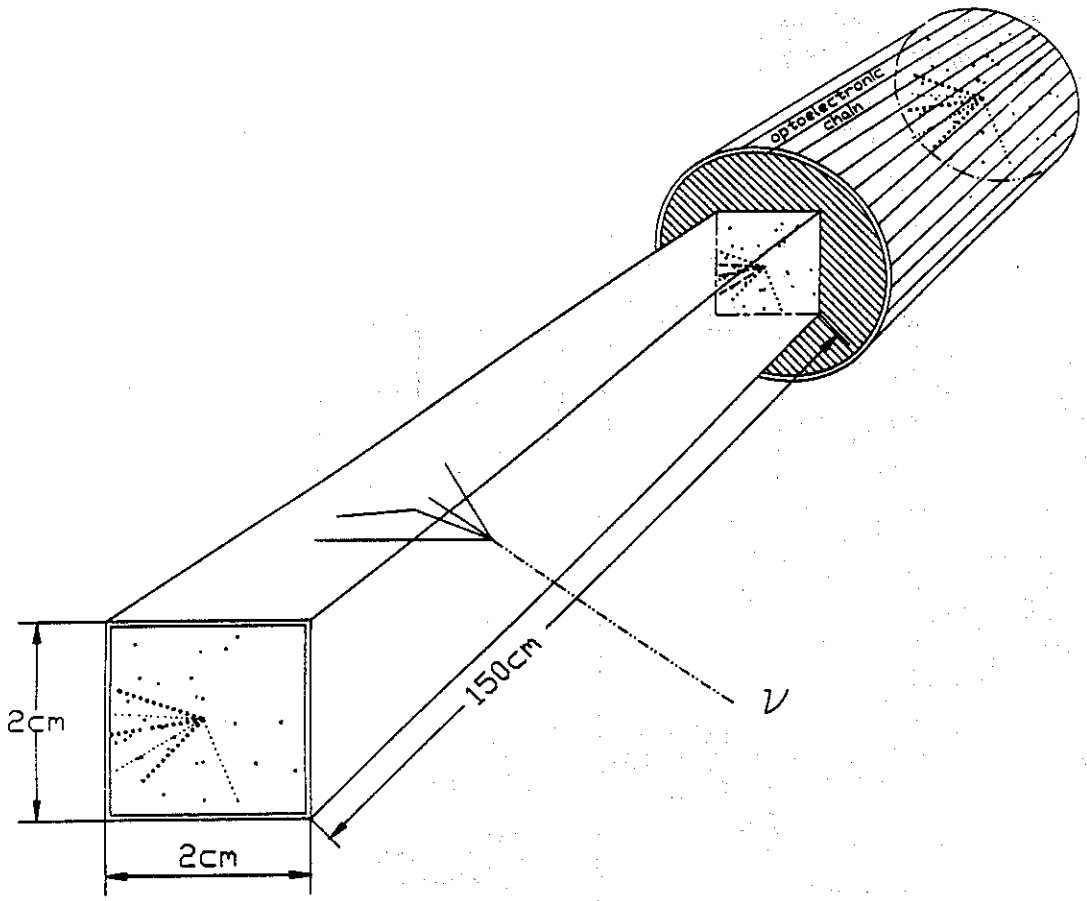

Figure 15(a)

Fiber target module oriented vertical to the incident neutrino beam.

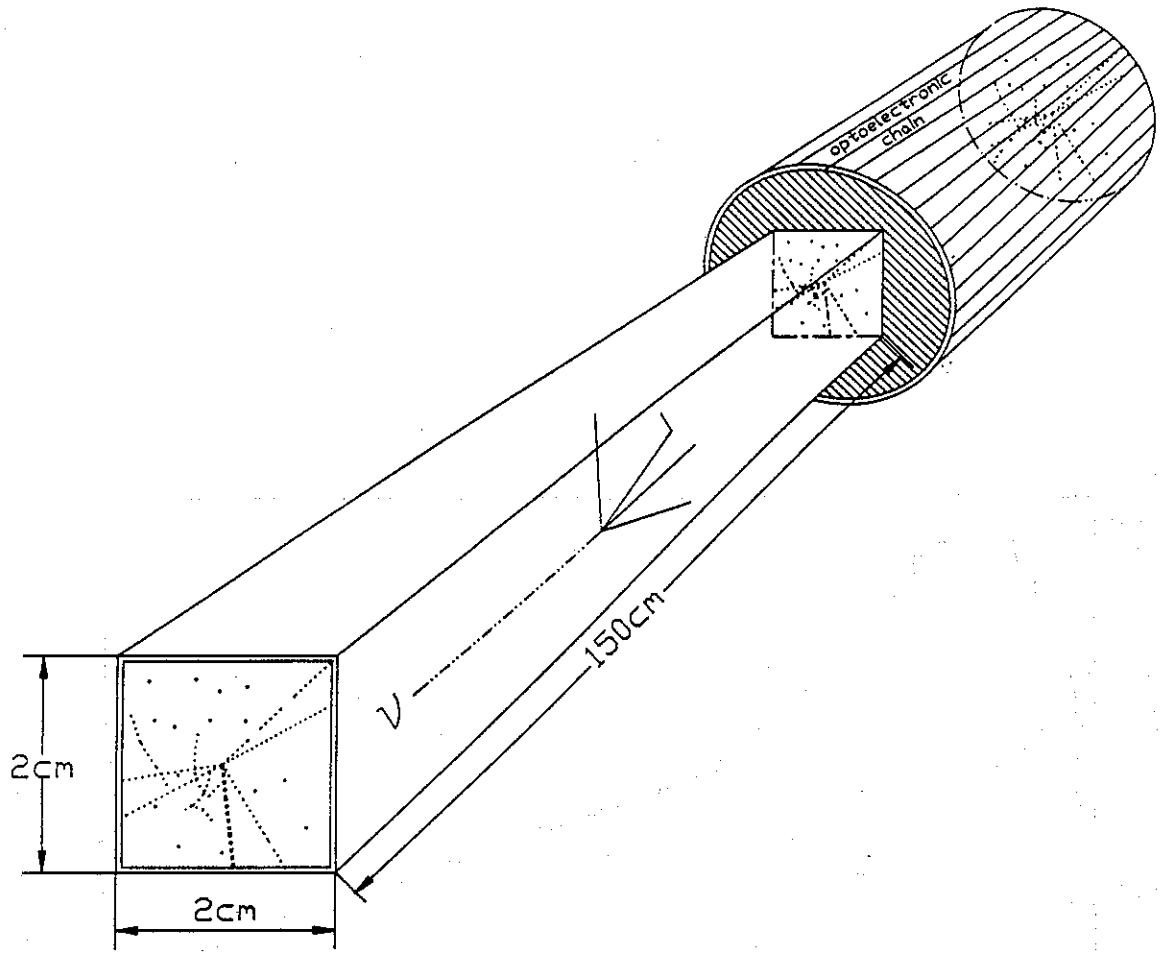

Figure 15(b)

Fiber target module oriented parallel to the incident neutrino beam.

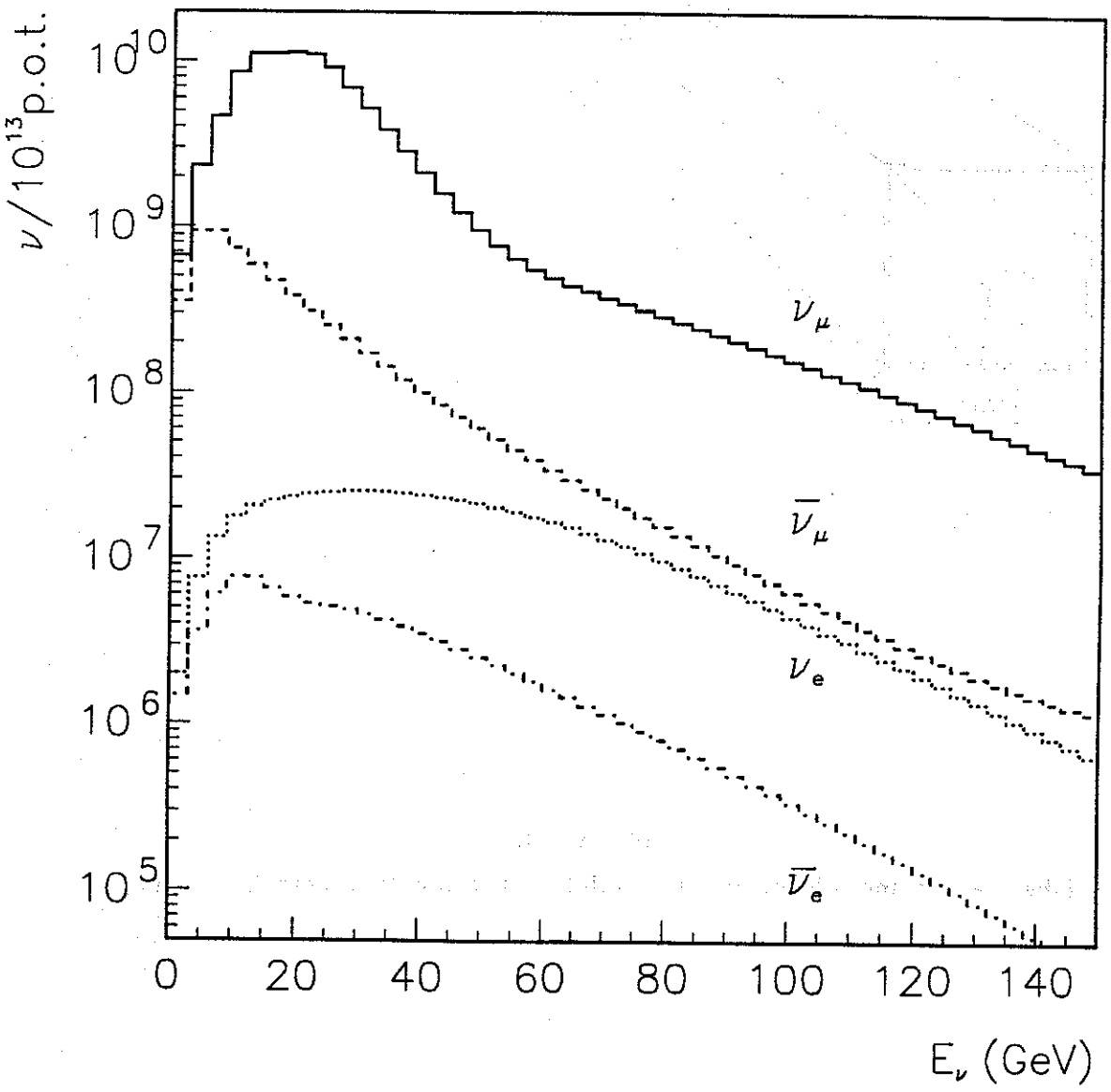

Figure 16

Flux spectra of the neutrino beam components (see also Table 4) over the area of the CHORUS detector $(1.44)^2$ m^2.

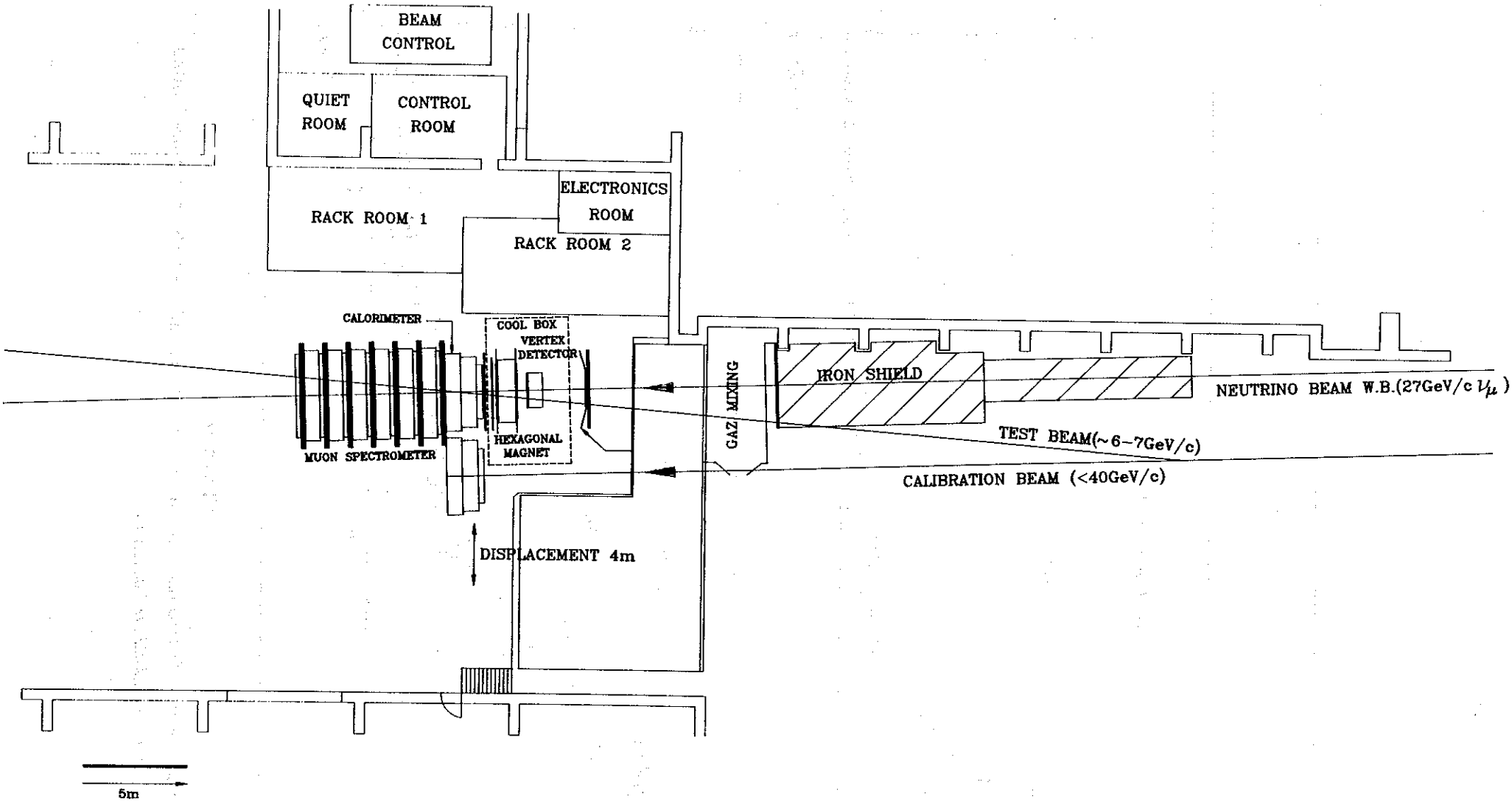

Figure 17

Layout of the experiment. Two branches of the test beam can be used alternatively.

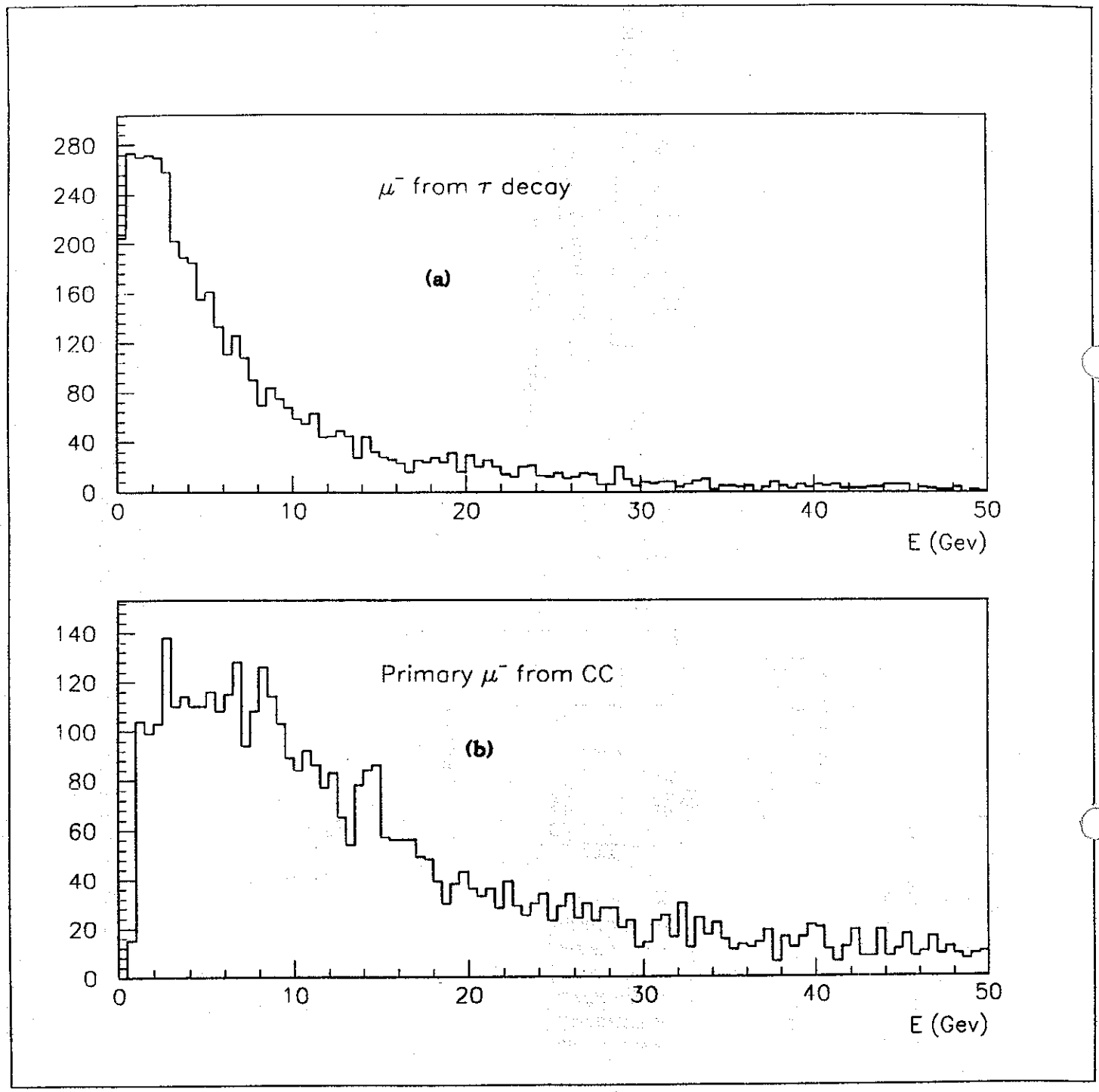

Figure 18

Muon energy distribution in (a) ν_τ and (b) ν_μ induced CC reaction folded with the resolution function.

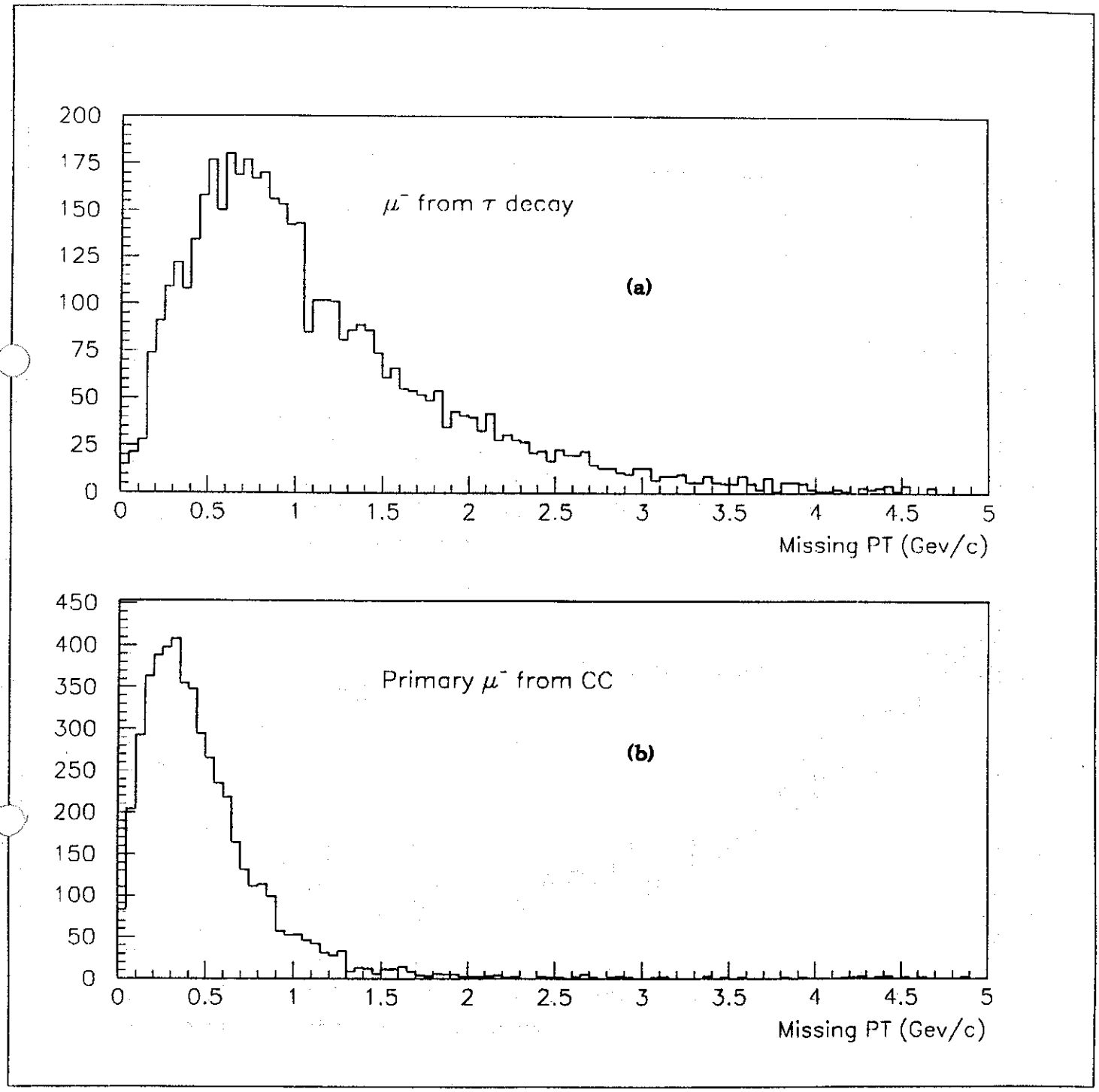

Figure 19

Missing transverse momentum distributions (a) for reaction $\nu_\tau N \rightarrow (\tau^- \rightarrow \mu)$ and (b) for reaction $\nu_\mu N \rightarrow \mu^- X$, including Fermi motion and resolutions.

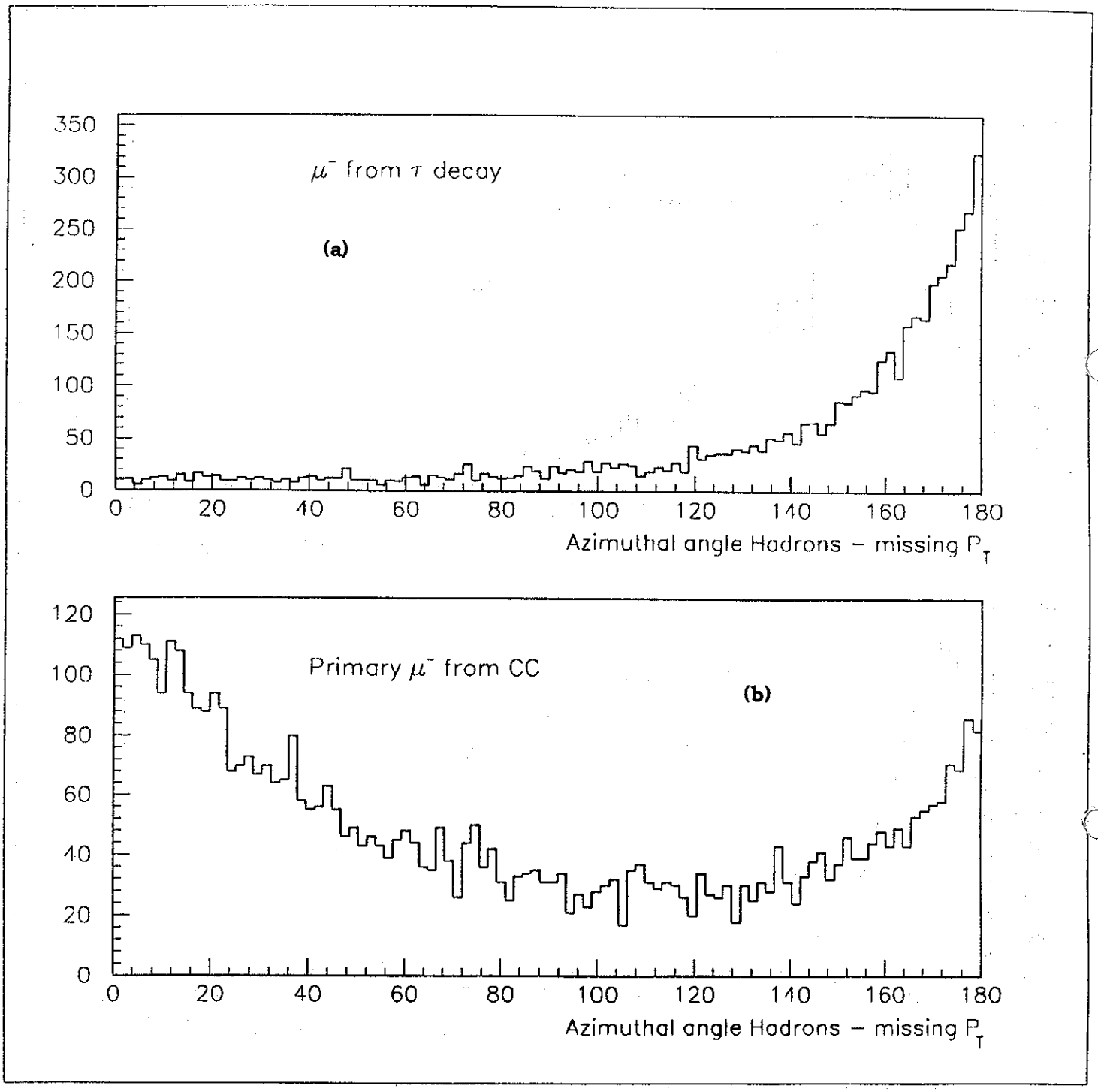

Figure 20

Distribution of the angle between the missing transverse momentum and the hadron shower direction (a) for $\nu_\tau N \Rightarrow (\tau^- \rightarrow \mu^-)X$ (b) for $\nu_\mu N \Rightarrow \mu^- X$, including Fermi motion and resolutions.

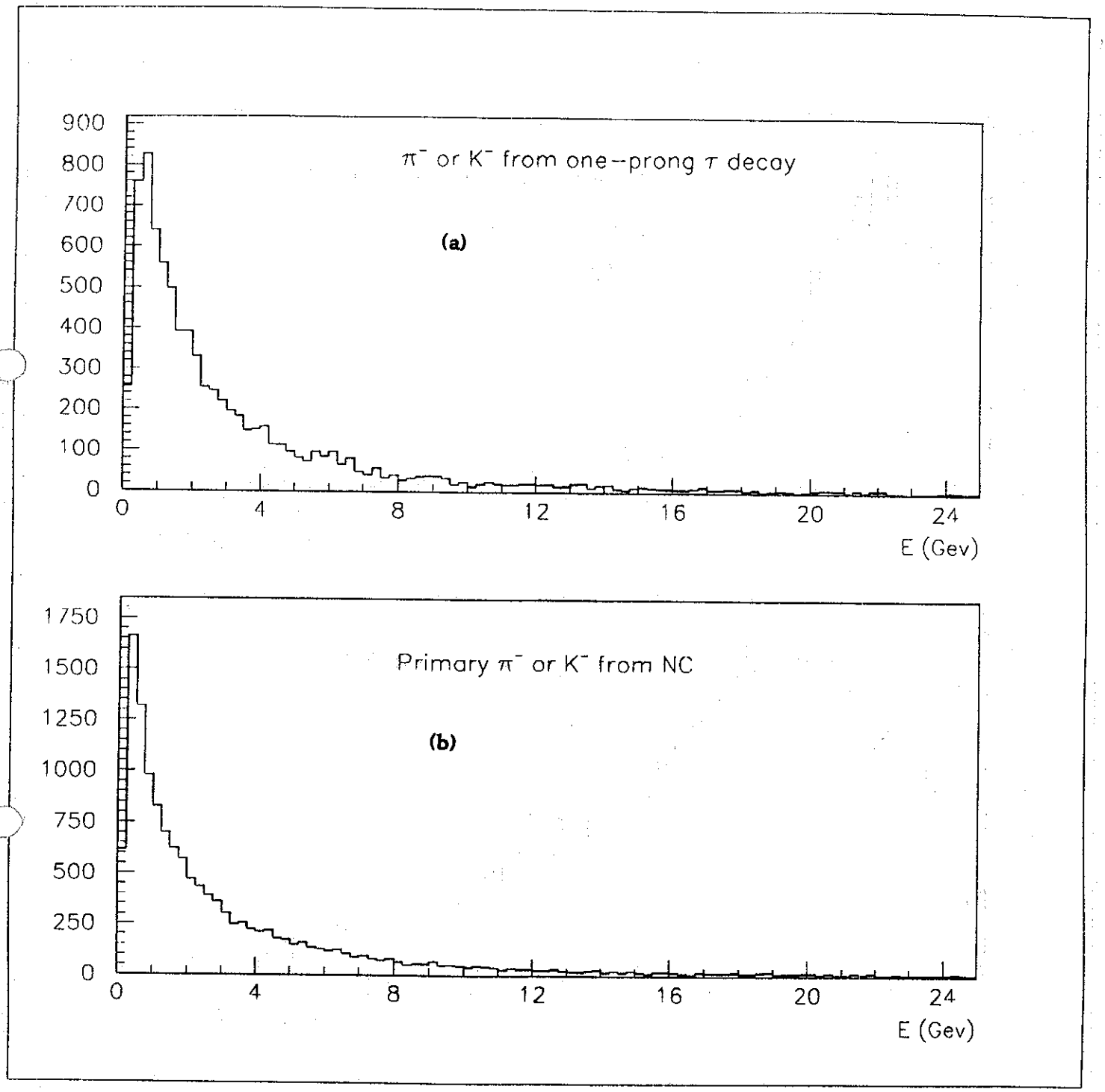

Figure 21

Energy distribution of negative hadrons (a) for $\nu_\tau N \rightarrow (\tau^- \rightarrow h^-)X$, (b) for $\nu_\mu N \rightarrow \nu_\mu h^- X$.

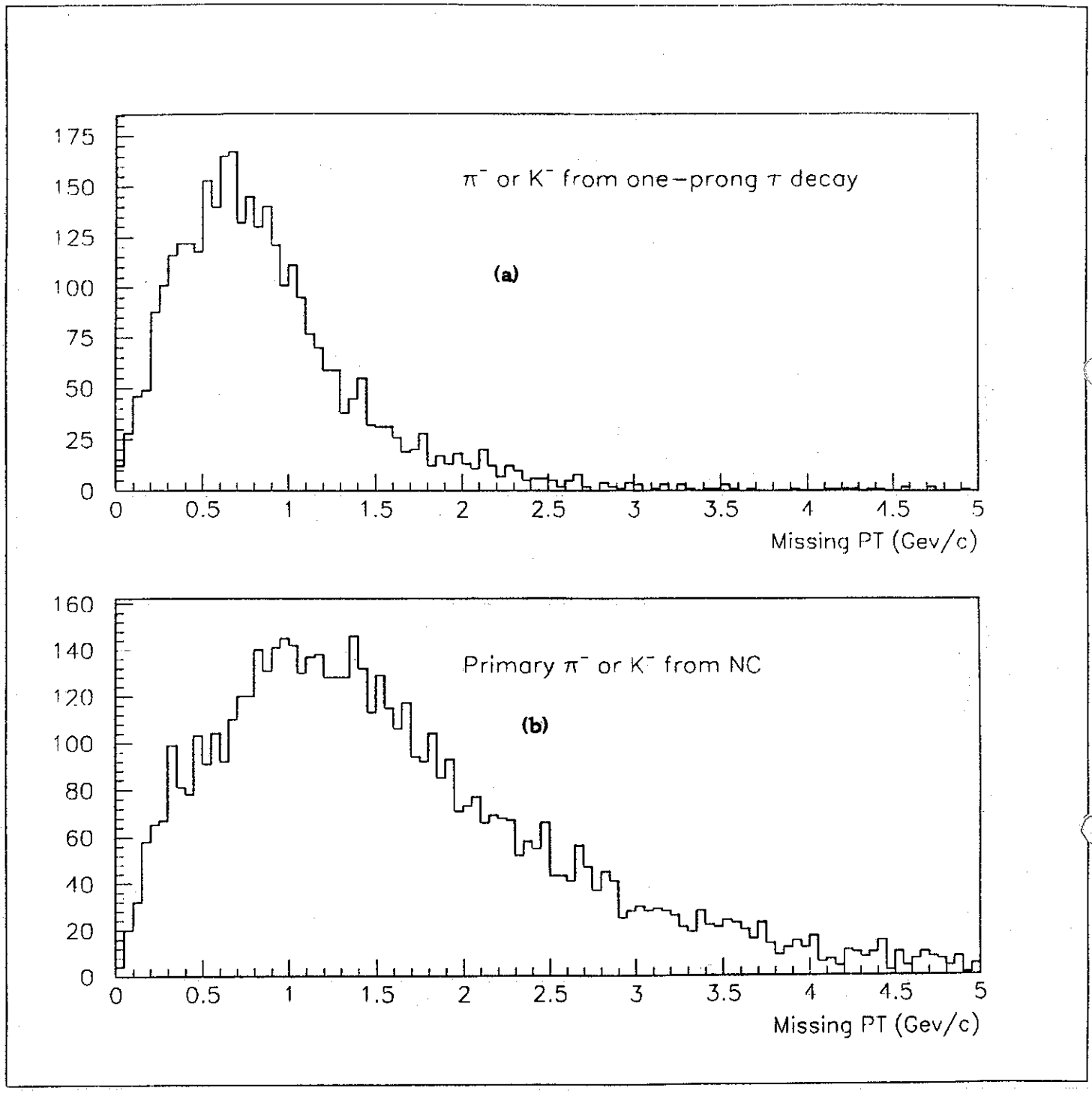

Figure 22

Missing transverse momentum distribution of negative hadrons (a) for $\nu_\tau N \rightarrow (\tau^- \rightarrow h^-)X$, (b) for $\nu_\mu N \rightarrow \nu_\mu h^- X$.

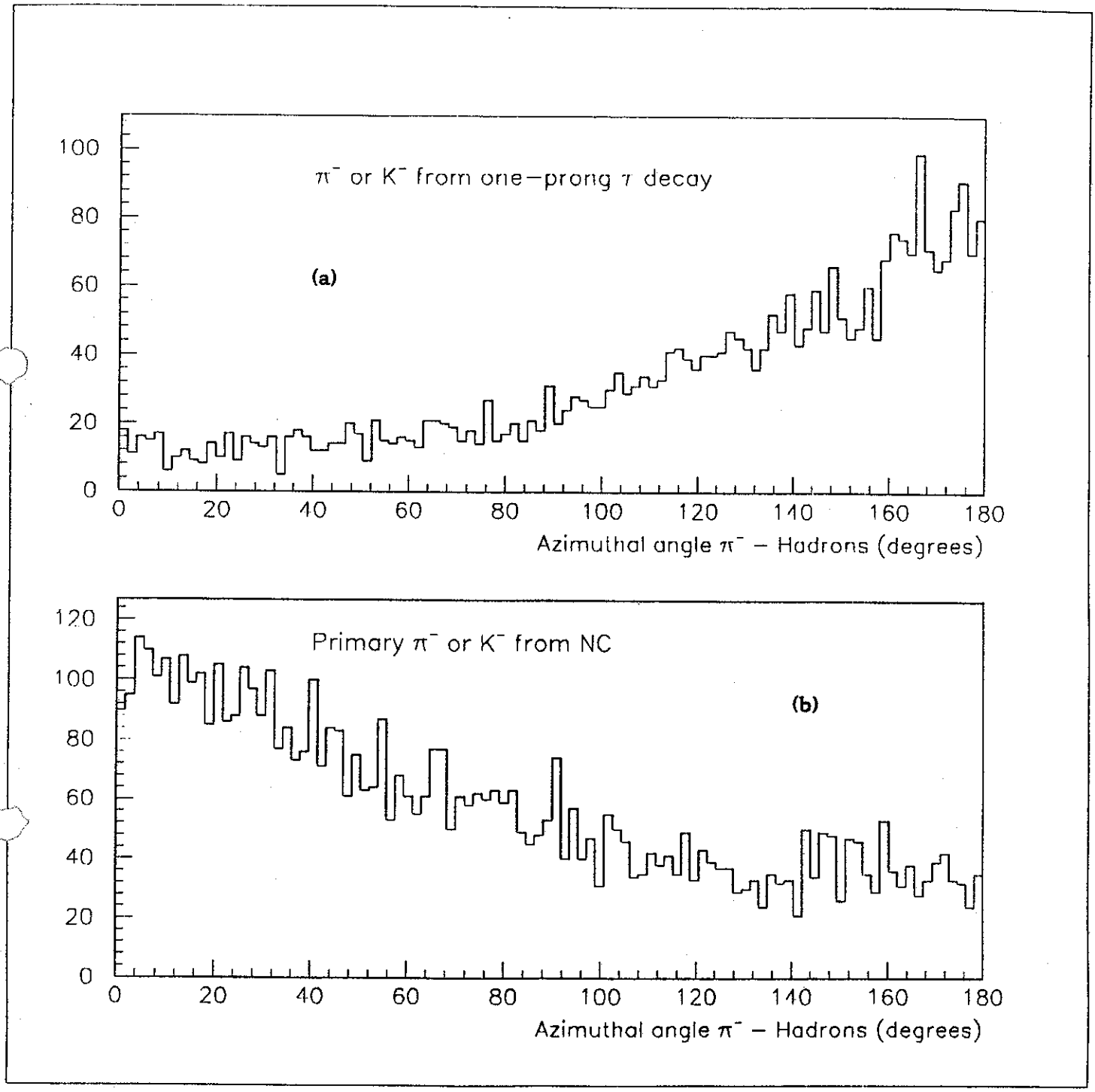

Figure 23

Azimuthal angle between h^- and the other hadrons (a) for $\nu_\tau N \rightarrow (\tau^- \rightarrow h^-) X$ (b) for $\nu_\mu N \rightarrow \nu_\mu h^- X$.